SWIRLING BIOCONVECTIVE NANOFLUID FLOW FROM A SPINNING STRETCHABLE DISK IN A PERMEABLE MEDIUM

J. C. Umavathi[1*], O. Anwar Bég[2], Tasveer A. Bég[3] and Ali Kadir[2].

[1]Department of Mathematics, Gulbarga University, Gulbarga-585 106, Karnataka, INDIA.
[2]Multi-Physical Engineering Sciences Group, Aeronautical/Mechanical Engineering, Salford University, School of Science, Engineering and Environment (SEE), Newton Building, Manchester, M54WT, UK.
[3]Engineering Mechanics Research, Israfil House, Dickenson Rd., Manchester, M13, UK.
Corresponding author- email: drumavathi@rediffmail.com

Abstract

Medical engineering is increasingly deploying nanotechnology and bio-inspired designs in the 21st century. Motivated by studying the spin coating of bio-nanofluid materials, gyrotactic bioconvection nanofluid swirling coating flow from a spinning disk to an isotropic permeable medium is analysed. The balance equations for mass, momentum, thermal, concentration and microorganism species including blowing effects are transformed into ordinary differential equations and then the solutions are obtained numerically through MATLAB bvp4c quadrature. These solutions are further validated with ADM (Adomian decompositions method). Increasing radial momentum slip reduces the radial skin friction and increasing tangential slip suppresses the tangential skin friction. Nusselt number, nanoparticle Sherwood number and micro-organism density number gradient are respectively decreased with increment in thermal slip, nanoparticle mass slip and micro-organism slip factors. Combinations of bioconvection and nanofluids provide excellent advantages in designing anti-bacterial and resilient bio-coatings for many devices.

Keywords Bio-inspired aqueous nano-coatings. Von Karman swirl. Gyrotactic micro-organisms. radial and circumferential slip; thermal slip. micro-organism slip. nanoparticle slip.

1.Introduction

In the 21st century engineers are increasingly deploying bioinspiration in numerous applications. Among these are medical coatings which are critical for many systems including surgical implants, surgical cutting tools (blades), face masks for pandemics and anti-bacterial interfaces. Many complex materials have been developed for coatings which exploit biological characteristics including bioactive glasses, bio-ceramics, hydroxyapatite coatings and multi-layered bio-embedded nanofilms [1]. A very efficient procedure for depositing complex coatings is spin coating. This technique deposits a constant thickness (uniform) film upon horizontal surfaces e.g. disks, via a centrifugal force which compels the coating fluid to spread over the surface [2]. Typically, precise and homogenous films with 1 to 10-micron thickness can be comfortably achieved. This technique is increasingly becoming popular for biological contamination-preventing coatings [3] and produces much better coating consistency than other methods such as dip coating and spray coating. Recent applications include platelet-rich plasma and adipose tissue-derived

microvascular fragment biological coatings which achieve enhanced biocompatibility [4]. Spin coating disk flows frequently feature Von Karman swirling [5] flows. By virtue of continuity, the liquid flows axially towards the disc to maintain radial flow. Von Kármán swirling flows are therefore fundamental to the intrinsic mechanisms of spin coating and analysis of such flows permits engineers to develop a deeper insight into the nature of coating deposition. Many investigations of Von Kármán swirling flows have therefore found in the recent literature. Ming *et al.* [6] studied the Von Kármán swirling flow of pseudoplastic/dilatant liquids from a rotating disk. In many studied, engineers have examined the free disk pumping effect wherein it is desirable to sustain a steady radial efflux of the fluid.

A major increasing deployment of nanotechnology is developed in this century. This includes nanoscale materials, nano-machines, nanorobotics etc. Nanofluids [7] are colloidal suspensions in liquids e.g. blood, biofluid, water, polymers, oils etc. The resulting system is therefore two-phase in nature and has been shown to offer significant thermal enhancement properties for a range of applications including nanomedicine (pharmacodynamics with gold nanoparticles), sterilization with silver nanoparticles, nano-fuels, cooling of bio-electronic circuits and many others. Nanofluids have also been embraced in biomedical coating where they have been shown to achieve enhanced anti-viral properties, high corrosion resistance, biocompatibility, osseointegration, durability and sustainability. Interesting studies include Lin *et al.* [8] nanostructured flexible fluoropolymer-based hybrid films [9], zinc-nanofluid based anti-corrosion coatings [10], gold mirror thin films for medical optical devices using photochemically prepared gold/polymer nano-coatings [11, 12], silicon nanoparticle coatings for biofuel cells [13] and copper nanoparticle aqueous coatings for infection control [14]. In parallel to clinical and experimental studies of nanofluids in medicine, computational studies have also received much attention. Two approaches have been embraced widely for simulating nanofluid dynamics. The Buongiorno model [15] is a *two-component* nanoscale model which includes a separate nanoparticle mass transfer balance equation, along with velocity and temperature conservation equations. However, it does not provide a framework for simulating actual nanoparticle types and is restricted therefore to a generic non-specific spherical nanoparticle. The alternative approach is the Tiwari-Das model [16] which is a *single-phase* model that neglects nanoparticle species diffusion but allows a robust platform for actual nanofluid properties via empirical relations. In the present study this model is adopted – *however a separate concentration equation is included to analyse nanoparticle mass diffusion, thereby refining the Tiwari-Das approach*. Swirling Von Karman flows of nanofluids from rotating disks have been studied extensively using the Tiwari-Das model, both for unitary (single nanoparticles) and hybrid (combined multiple nanoparticles). Tassaddiq *et al.* [17] adopted Tiwari-Das model over a rotating magnetised hybrid nanofluids. They examined CNTs and Fe_3O_4 nanoparticles and noted superior thermal performance of $CNT + Fe_3O_4/H_2O$ compared with only (Fe_3O_4)-water, and also observed

substantial flow acceleration and temperature elevation with increasing disk rotational velocity. Hafeez *et al.* [18] used the BVP Midrich numerical scheme in Maple to simulate the swirling Oldroyd-B nanofluid flow from an axially symmetric rotating disk under a vertical applied magnetic field. Shamshuddin *et al.* [19] investigated the Marangoni hydromagnetic nanofluids convection with radiative heat flux effects.

A mathematical model to study the thermally fully developed pressure-driven flow of Newtonian fluid in a finite length vertical microtube with a spatial–temporal dependent membrane contraction, was studied by Bhandari and Tripathi [20]. They concluded that the temperature elevated upto 49% in microtube by the presence of heat source and entropy was controlled by membrance shape and relative temperature. Tripathi et al. [21] investigated how temperature affected virus transmission in peristaltic blood vessels and how virus density and particle diameter affected the transmission of the virus from an infected person to a non-infected person. The observation made was that the temperature played a significant role in reducing the package density of the virion droplet, i.e., the cohesion of the particles was reduced with an increment in temperature, so that the SARS-CoV-2 takes greater time to affect the body. Transient analysis for heat and mass transfer in a finite length vertical microchannel was presented by Bhandari et al. [22]. They found that the pressure was generated due to the kinematic of membrane motion and controlled by the thermal effects and buoyancy force.

There are many mechanisms encountered in nature, for internal and external propulsion, including flapping motions, peristaltic pumping, ciliated metachronal assisted transport etc. Another mechanism deployed by micro-organisms is known as *bioconvection*. This arises due to differences in density of the self-propelled micro-organisms usually in water and many types exist depending on the specific taxis (stimulus) involved, including photo-tactic (light-driven), chemo-tactic (e.g. oxygen-driven), magneto-tactic (magnetic field-driven), geo-tactic (gravity-driven) and gyrotactic (torque-driven) bioconvection [23]. As a result bioconvection fluid dynamics has emerged as a very rich area of modern viscous flows and is analyzed as a classic system wherein *macroscopic phenomena* are generated via *microscopic cellular behavior* in relatively dilute aqueous systems. In addition to the obvious ecological occurrence of bioconvection e.g. algae in oceans, bioconvection is also being exploited in engineering systems. Recent developments in this regard include green algae-based fuel cells, anti-corrosion interfaces and biologically enhanced coatings in the medical industry [24]. Engineers have also explored the combination of bioconvection with nanofluids to achieve yet further improvements in sustainable and resilient coatings. In particular, mathematical modelling studies of combined bioconvection nanofluid coating flows, have received considerable attention. These studies have often considered the swimming alga, *Chlamydomonas nivalis and the Tiwari-Das model.* Ferdows *et al.* [25] used the CodeBlocks Fortran platform to compute the bioconvection nanofluid flow from a contracting/extending coating surface with variable thermophysical properties.

Akram et al. [26] investigated the fluid flow analysis and the heat transfer characteristics of 10 W40-based titanium dioxide nanofluid subject to electroosmotic forces and the peristaltic propulsion in a curved microchannel. They revealed that the temperature of the nanofluid drops for a larger curvature parameter which physically corresponds to a less curved channel. Further, the electroosmotic flow parameters have a progressive impact on the velocity and the convective heat transfer process. The mathematical modeling of the electroosmotically boosted peristaltic propulsion of water-based silver nanofluid through an asymmetric channel was researched by Akram et al. [27]. They found that for larger temperature differences within a fluid medium, the Nusselt number declines in the case where the modified Buongiorno model was utilized whereas the Tiwari-Das model does not include the effect of temperature difference. Sridhar et al. [28] proposed a mathematical model tow-dimensional motion of the couple stress nanofluid using gold nanopartilces under the application of peristaltic propulsion and electroosmosis mechanisms in an asymmetric microchannel. They noticied that sphere-shaped gold nanoparticles enhance the temperature as compared to other geometries of nanoparticles. Akram et al. [29] investigated the effect of boron nitride nanotubes suspension on the heat transfer performance of ethylene glycol based nanofuids flow curved microchannel driven by two pumping mechanisms. They found that more cooling effect was generated by considering a channel with relatively less curvature and fluid momentum was assisted by the larger curvature parameter. Akram et al. [30] compared the heat transfer performance of two different nanofluid flowing through a symmetric microchannel which is pumped by the mechanism of peristalsis and electroosmosis. The two nanoluids were carboxy-methyl-cellulose (CMC) + water-based molybdenum dioxide (MoS_2) nanofluid and kerosene oil-based molybdenum dioxide nanofluid. They found that upon increasing electroosmotic parameters, there is a very minute rise in volumetric entropy generation in the case of MoS_2/CMC + water nanofluid. However, there was substantial rise in entropy generation for MoS_2/kerosene oil nanofluid. Akram et al. [31] analyzed the flow of single-walled carbon nanotubes (SWCNTs) suspended water-based ionic solution driven by combined effects of electroosmosis and peristalsis mechanisms. Improvement in thermal conductivity of base fluid was noticed with increasing SWCNTs volume fraction and the axial velocity magnifed with Helmholtz–Smoluchowski velocity. The influence of Coriolis body force, electro-magnetohydrodynamics (EMHD) and thermal radiative heat transfer on the Casson hybrid mixed convection nanofluid driven by an exponentially accelerated plate adjacent to a porous medium in a rotating system was analysed by Tripathi et al. [32]. Saleem et al. [33] studied the entropy of hybrid nanofluids flow driven by cilia beating. They revealed that high electric potential can reduce the entropy during the radiated hybrid nanofluids flow in microchannel. Javid et al. [34] explored the influence of magnetic field on double-diffusive convection in complex biomimetic (peristaltic) propulsion of nanofluid through a two-dimensional divergent channel. The conclusions drawn was that the bolus circulations disappeared from trapping phenomena for larger strength of

magnetic and porosity medium. The computational modeling approach to analyze the peristaltic pumping of couple stress hybrid nanofluids regulated by the electroosmosis mechanism through a microchannel was researched by Tripathi et al. [35] and claimed that the maximum axial velocity and nanoparticle temperature occur in water–titanium dioxide as compared with water–silver.

Acharya [36] researched on the flow pattern and thermal scenario of a nanofluid spraying on an inclined permeable rotating disk. He found that heat transport was enhanced for nanolayers, but reduced heat transmission for nanoparticles' diameter. Entropy generation investigation of hybrid nanofluidic transport over an unsteady spinning disk was reported by Acharya et al. [37]. Their findings showed that the entropy generation was augmented for higher magnetic value but reduced for velocity slip, radiation, and nanoparticle concentration. Hybrid nanofluid gave a lower magnitude in entropy production as compared to the usual nanofluid. Acharya et al [38] also studied the impact of a higher-order chemical reaction and second-order slip on the bioconvective nanoliquid flow comprising gyrotactic microorganisms between two squeezed parallel plates. Their results communicated that temperature diminished for squeezing factor and first-order velocity slip parameter, but augmented for second-order slip parameter. The hydrothermal features of chemically reactive nanofluidic transport over an inclined spinning disk was investigated by Acharya [39]. His outcomes assured that the normalized thickness parameter augmented the radial velocity and nanoparticle concentration. Chemical reaction reduced the concentration profile for suction but amplified for injection.

In this article we combine nanofluid and gyrotactic bioconvection to study bio-nano swirl coating flows. As noted earlier, spin coating processes feature rotational body forces. Computational studies of rotating bioconvection nanofluid flow involve the simultaneous consideration of Centrifugal forces, nanofluid flow and micro-organism bioconvection, and all three must be analysed to model spin coating flows of bio-nano-coatings. Kadir *et al.* [40] deployed the Buongiorno model, shooting quadrature and generalized differential quadrature to simulate the bioconvection swirling oxytactic nanofluid flow from a radially stretching spinning disk. Xun *et al.* [41] employed Matlab bvp4c software to find the solutions for the swirling flow between two rotating plates for variable properties. They noted that considerable modification in local rate of heat trnafer and wall motile microorganism flux is achieved with an increment in thermal conductivity variation parameter. The enlargement of Péclet number produces higher concentrations in the dual disk core region. Waqas *et al.* [42] used bvp4c Matlab quadrature to study numerically the gyrotactic viscoplastic bioconvection nanofluid over a rotating disk under radiative flux with multiple slip boundary conditions. They observed that radial and tangential flow deceleration is produced with higher bioconvection Rayleigh number whereas greater thermophoresis parameter enhances temperatures and nanoparticle concentrations. Khan et al. [43] studied Stefan blowing effects in swirling bioconvective nanofluid

flow from a rotating and stretchable disk respectively. Therefore once can conclude from the above cited papers that there is a magnificent benefits of amalgamating micro-organism bioconvection with nanofluids for improving heat and mass transfer characteristics.

In many manufacturing flow operations aimed at producing anti-viral and anti-fouling biological coatings, *slip effects* arise. This relates to the non-adherence of the coating fluid to the substrate and therefore invalidates the classical no-slip boundary condition. In bio-nano-coatings, often key considerations are extreme hydrophilic , electrostatic repellence, characteristics and surfaces with self-polishing (for example for surgical tools and implants). All these require consideration of complex slip conditions in mathematical models. A further advantage of such coatings is their ability to mitigate microbial adhesion and produce exceptional sterilization. Many excellent studies of slip hydrodynamics in coating flows have been communicated. Further studies include Eijkel (on micro-nano fluidic medical devices) and Ngamaramvaranggul and Webster [44] (who implemented finite element method to simulate slip effects in wire coating flows). Rotating disk hydromagnetic nanofluid slip flow was researched by Hayat *et al.* [45]. Zohra et al. [46] scrutinised the bioconvection magnetized nanofluid flow from a spinning conical body using multiple slip effects.

In this article, an investigation is carried out to understand the bioconvection gyrotactic nanofluid swirling coating flow Vafai [47] from a spinning disk to an isotropic permeable medium. Darcy's law is adopted for bulk porous medium drag effects. The disk is also assumed to stretch radially Yin et al. [48]. The Tiwari-Das and Kuznetsov models are used to simulate nanofluid and bioconvection phenomena. An additional concentration equation is however included for nanoparticles. Anisotropic hydrodynamic slip (radial and tangential) at the disk surface is also considered in addition to thermal slip, nanoparticle mass slip and micro-organism slip at the disk surface. Blowing effects due to concentration are incorporated. The transformed, dimensionless boundary layer differential equations with suitable conditions on the boundary are computed with MATLAB bvp4c quadrature Bég et al. [49]. Verification of the MATLAB solutions with previous studies Bég et al. [50] and Chen et al.[51] is also presented. The validation of the model with the ADM is also performed Adomian [52]. Aqueous base fluid is considered, and *five different nanoparticles* are investigated- i.e. *silver (Ag), copper (Cu), Titania (TiO₂), diamond (C) and silicon oxide (SiO₂)*. Comprehensive graphs are presented for the effects of pertinent parameters on the momentum, energy, nanoparticle concentration and motile micro-organism density number. The novelty of this analysis is that it generalizes earlier studies Bég et al. [50] to consider multiple nanoparticles to provide a comparison of actual performance characteristics for spin coating flows. Therefore, it is envisaged that the present study will be relevant to providing further understanding of the complex flow characteristics in Von Karman swirl spin coated bio-nanofilms for implants, anti-bacterial interfaces (Durual et al.[53] etc.).

2. Spin bio-nano coating Von Karman swirl flow model

The spin coating flow regime to be studied is depicted in **Fig. 1**. Axisymmetric, incompressible nanofluid swirling flow occurs from a spinning horizontal radially stretching disk to a saturated permeable medium involving gyrotactic micro-organisms (e.g. filter biomaterial). The porous medium is rigid, isotropic, homogenous and obeys the Darcy law. The nanoparticles and micro-organisms and nanoparticles do not connect and the nanofluid is dilute and aqueous. Disk edge effects are neglected. $(\bar{r}, \theta, \bar{z})$ represents the cylindrical co-ordinates and Ω represents the angular velocity along the vertical axis. Radial, tangential and axial velocity components are respectively $(\bar{u}, \bar{v}, \bar{w})$. Both radial and tangential momentum slip i.e. anisotropic hydrodynamic is considered. At the disk surface only isotropic thermal, nanoparticle mass and motile micro-organism slip is included. Stefan blowing effects are also prescribed at the disk surface. The disk stretching rate is proportional to a power-law velocity, of exponent, *m*. The governing boundary layer conservation equations are modified from Bég *et al*. [50] and may be shown to be:
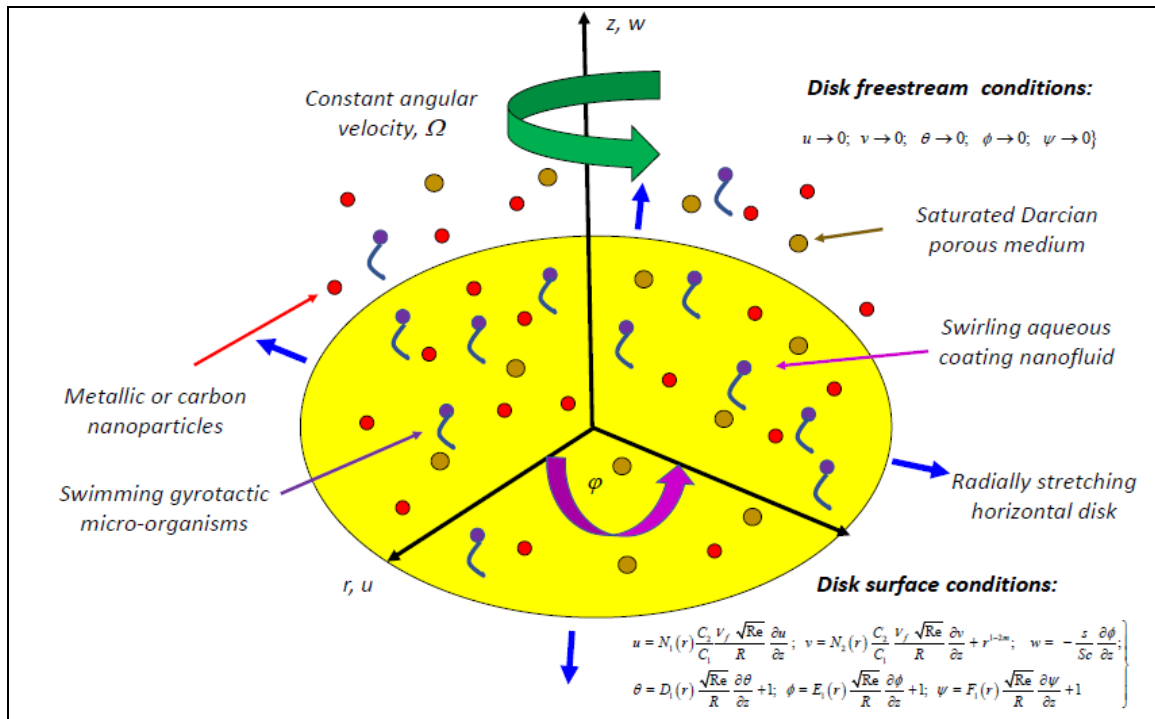
Fig 1: Bio-nano-coating swirling anisotropic slip flow in a Darcian porous medium

Mass conservation (continuity):

$$\frac{1}{\bar{r}} \frac{\partial}{\partial \bar{r}} \left(\bar{r}\,\bar{u} \right) + \frac{\partial \bar{w}}{\partial \bar{z}} = 0 \tag{1}$$

Momentum conservation (radial, tangential and axial):

$$\bar{u}\,\frac{\partial \bar{u}}{\partial \bar{r}} + \bar{w}\,\frac{\partial \bar{u}}{\partial \bar{z}} - \frac{\bar{v}^2}{\bar{r}^2} = \frac{\mu_{nf}}{\rho_{nf}}\left(\frac{\partial^2 \bar{u}}{\partial \bar{r}^2} + \frac{1}{\bar{r}^2}\frac{\partial \bar{u}}{\partial \bar{r}} + \frac{\partial^2 \bar{u}}{\partial \bar{z}^2} - \frac{\bar{u}}{\bar{r}^2}\right) - \frac{\mu_{nf}}{\rho_{nf}\,K\!\left(\dfrac{\bar{r}}{R}\right)}\,\bar{u} \qquad (2)$$

$$\bar{u}\,\frac{\partial \bar{v}}{\partial \bar{r}} + \bar{w}\,\frac{\partial \bar{v}}{\partial \bar{z}} - \frac{\bar{u}\,\bar{v}}{\bar{r}^2} = \frac{\mu_{nf}}{\rho_{nf}}\left(\frac{\partial^2 \bar{v}}{\partial \bar{r}^2} + \frac{1}{\bar{r}}\frac{\partial \bar{v}}{\partial \bar{r}} + \frac{\partial^2 \bar{v}}{\partial \bar{z}^2} - \frac{\bar{v}}{\bar{r}^2}\right) - \frac{\mu_{nf}}{\rho_{nf}\,K\!\left(\dfrac{\bar{r}}{R}\right)}\,\bar{v} \qquad (3)$$

$$\bar{u}\,\frac{\partial \bar{w}}{\partial \bar{r}} + \bar{w}\,\frac{\partial \bar{w}}{\partial \bar{z}} = \frac{\mu_{nf}}{\rho_{nf}}\left(\frac{\partial^2 \bar{w}}{\partial \bar{r}^2} + \frac{1}{\bar{r}}\frac{\partial \bar{w}}{\partial \bar{r}} + \frac{\partial^2 \bar{w}}{\partial \bar{z}^2}\right) \qquad (4)$$

Energy (heat) conservation:

$$\bar{u}\,\frac{\partial \bar{T}}{\partial \bar{r}} + \bar{w}\,\frac{\partial \bar{T}}{\partial \bar{z}} = \frac{k_{nf}}{\left(\rho C_p\right)_{nf}}\left(\frac{\partial^2 \bar{T}}{\partial \bar{r}^2} + \frac{1}{\bar{r}}\frac{\partial \bar{T}}{\partial \bar{r}} + \frac{\partial^2 \bar{T}}{\partial \bar{z}^2}\right) \qquad (5)$$

Nanoparticle Concentration conservation:

$$\bar{u}\,\frac{\partial \bar{C}}{\partial \bar{r}} + \bar{w}\,\frac{\partial \bar{C}}{\partial \bar{z}} = D\left(\frac{\partial^2 \bar{C}}{\partial \bar{r}^2} + \frac{1}{\bar{r}}\frac{\partial \bar{C}}{\partial \bar{r}} + \frac{\partial^2 \bar{C}}{\partial \bar{z}^2}\right) \qquad (6)$$

Conservation of density number of motile organisms:

$$\bar{u}\,\frac{\partial \bar{n}}{\partial \bar{r}} + \bar{w}\,\frac{\partial \bar{n}}{\partial \bar{z}} + \frac{\partial}{\partial \bar{z}}\left(\bar{n}\,\tilde{v}\right) = D_n\left(\frac{\partial^2 \bar{n}}{\partial \bar{r}^2} + \frac{1}{\bar{r}}\frac{\partial \bar{n}}{\partial \bar{r}} + \frac{\partial^2 \bar{n}}{\partial \bar{z}^2}\right) \qquad (7)$$

The appropriate boundary conditions are [50]:

At $\bar{z} = 0$: (disk surface),

$$\bar{u} = N_1\!\left(\frac{\bar{r}}{R}\right)\frac{\mu_{nf}}{\rho_{nf}}\frac{\partial \bar{u}}{\partial \bar{z}}, \qquad \bar{v} = N_2\!\left(\frac{\bar{r}}{R}\right)\frac{\mu_{nf}}{\rho_{nf}}\frac{\partial \bar{v}}{\partial \bar{z}} + \left(\frac{\bar{r}}{R}\right)^{1-2m}\Omega\,R, \qquad \bar{w} = -\frac{D}{1-C_w}\frac{\partial \bar{C}}{\partial \bar{z}},$$

$$\bar{T} = T_w + D_1\!\left(\frac{\bar{r}}{R}\right)\frac{\partial \bar{T}}{\partial \bar{z}}, \qquad \bar{C} = C_w + E_1\!\left(\frac{\bar{r}}{R}\right)\frac{\partial \bar{C}}{\partial \bar{z}}, \qquad \bar{n} = n_w + F_1\!\left(\frac{\bar{r}}{R}\right)\frac{\partial \bar{n}}{\partial \bar{z}}. \qquad (8)$$

As $\bar{z} \to +\infty$ (free stream),

$$\bar{u} \to 0,\ \ \bar{v} \to 0,\ \ \bar{T} \to T_\infty,\ \ \bar{C} \to C_\infty,\ \ \bar{n} \to n_\infty \qquad (9)$$

The Tiwari-Das model is to be deployed for nanofluid properties. This neglects the thermophoresis and Brownian motion effects associated with the Buongiorno model (Buongiorno [15]). The appropriate relations are given in due course. In the above Eqns. (1)-(9) are temperature (T), number of motile organisms (n), concentration (C), viscosity of the nanofluid (μ_{nf}), density of the nanofluid (ρ_{nf}), constant permeability of porous medium (K_0), variable permeability $(K = K_0\,r^{2m})$, heat capacity of the base fluid $(\rho C_p)_f$, heat capacity of the nanofluid $(\rho C_p)_{nf}$,

thermal conductivity of the nanofluid $\left(k_{nf}\right)$, reference scale length (R), surface temperature $\left(T_w\right)$, ambient temperature $\left(T_\infty\right)$, microorganism diffusion coefficient $\left(D_n\right)$, ambient nanoparticle mass concentration $\left(C_\infty\right)$, surface nanoparticle mass concentration $\left(C_w\right)$, nanoparticle mass slip factor $\left(E_1 = \left(E_1\right)_0 \, r^m\right)$, gyrotactic microorganism slip $\left(F_1 = \left(F_1\right)_0 \, r^m\right)$, radial velocity slip along $\bar{u}$ $\left(N_1 = \left(N_1\right)_0 \, r^m\right)$, tangential velocity slip along $\bar{v}$ $\left(N_2 = \left(N_2\right)_0 \, r^m\right)$, thermal slip factor $\left(D_1 = \left(D_1\right)_0 \, r^m\right)$, maximum cell swimming speed $\left(W_c\right)$, chemotaxis constant $\left(\tilde{b}\right)$, average directional swimming velocity of gyrotactic micro-organisms $\left(\tilde{v} = \dfrac{\tilde{b} \, W_c}{\Delta C} \dfrac{\partial \bar{C}}{\partial \bar{z}}\right)$, wall motile micro-organism density number $\left(n_w\right)$ and stretching rate power law exponent m respectively.

The nonlinear partial differential boundary value problem defined by Eqns. (1)-(9) are formidable to solve using numerical methods. The following relations are implemented to furnish the equations in non-dimensional form as in Bég *et al.* [50]

$$r = \frac{\bar{r}}{R}, \quad z = \frac{\bar{z}}{R}\sqrt{\mathrm{Re}}, \quad u = \frac{\bar{u}}{\Omega R}, \quad v = \frac{\bar{v}}{\Omega R}, \quad w = \frac{\bar{w}}{\Omega R}\sqrt{\mathrm{Re}},$$
$$\psi = \frac{\bar{n}}{n_w}, \quad \theta = \frac{\bar{T} - T_\infty}{T_w - T_\infty}, \quad \phi = \frac{\bar{C} - C_\infty}{C_w - C_\infty} \tag{10}$$

Implementing Eqn. (10) the *non-dimensional* boundary layer equations emerge as:

$$\frac{\partial u}{\partial r} + \frac{u}{r} + \frac{\partial w}{\partial z} = 0 \tag{11}$$

$$u\frac{\partial u}{\partial r} + w\frac{\partial u}{\partial z} - \frac{v^2}{r} = \frac{C_2}{C_1 \, \mathrm{Re}}\left(\frac{\partial^2 u}{\partial r^2} + \frac{1}{r}\frac{\partial u}{\partial r} - \frac{u}{r^2}\right) + \frac{C_2}{C_1}\frac{\partial^2 u}{\partial z^2} - \frac{C_2}{C_1}\frac{1}{\rho\Omega K_0 \, r^{2m+1}} u \tag{12}$$

$$u\frac{\partial v}{\partial r} + w\frac{\partial v}{\partial z} + \frac{uv}{r} = \frac{C_2}{C_1 \, \mathrm{Re}}\left(\frac{\partial^2 v}{\partial r^2} + \frac{1}{r}\frac{\partial v}{\partial r} - \frac{v}{r^2}\right) + \frac{C_2}{C_1}\frac{\partial^2 v}{\partial z^2} - \frac{C_2}{C_1}\frac{1}{\rho\Omega K_0 \, r^{2m+1}} v \tag{13}$$

$$u\frac{\partial w}{\partial r} + w\frac{\partial w}{\partial z} = \frac{C_2}{C_1 \, \mathrm{Re}}\left(\frac{\partial^2 w}{\partial r^2} + \frac{1}{r}\frac{\partial w}{\partial r}\right) + \frac{C_2}{C_1}\frac{\partial^2 w}{\partial z^2} \tag{14}$$

$$u\frac{\partial \theta}{\partial r} + w\frac{\partial \theta}{\partial z} = \frac{C_3}{C_4 \, \mathrm{Pr} \, \mathrm{Re}}\left(\frac{\partial^2 \theta}{\partial r^2} + \frac{1}{r}\frac{\partial \theta}{\partial r}\right) + \frac{C_3}{C_4 \, \mathrm{Pr}}\frac{\partial^2 \theta}{\partial z^2} \tag{15}$$

$$u\frac{\partial \phi}{\partial r} + w\frac{\partial \phi}{\partial z} = \frac{1}{Sc \, \mathrm{Re}}\left(\frac{\partial^2 \phi}{\partial r^2} + \frac{1}{r}\frac{\partial \phi}{\partial r}\right) + \frac{1}{Sc}\frac{\partial^2 \phi}{\partial z^2} \tag{16}$$

$$u\frac{\partial \psi}{\partial r} + w\frac{\partial \psi}{\partial z} = \frac{1}{Sb}\frac{\partial^2 \psi}{\partial z^2} + \frac{1}{\mathrm{Re} \, Sb}\left(\frac{\partial^2 \psi}{\partial r^2} + \frac{\partial \psi}{\partial r}\right) - \frac{Pe}{Sb}\left(\frac{\partial \psi}{\partial z}\frac{\partial \phi}{\partial z} + \psi\frac{\partial^2 \phi}{\partial z^2}\right) \tag{17}$$

The dimensionless boundary conditions at the disk surface and in the free stream (edge of the boundary layer) take the form:

$$u = N_1(r)\frac{C_2}{C_1}\frac{v_f}{R}\frac{\sqrt{\mathrm{Re}}}{\partial z}\frac{\partial u}{\partial z} ; \quad v = N_2(r)\frac{C_2}{C_1}\frac{v_f}{R}\frac{\sqrt{\mathrm{Re}}}{\partial z}\frac{\partial v}{\partial z} + r^{1-2m}; \quad w = -\frac{s}{Sc}\frac{\partial \phi}{\partial z};$$

$$\theta = D_1(r)\frac{\sqrt{\mathrm{Re}}}{R}\frac{\partial \theta}{\partial z}+1; \quad \phi = E_1(r)\frac{\sqrt{\mathrm{Re}}}{R}\frac{\partial \phi}{\partial z}+1; \quad \psi = F_1(r)\frac{\sqrt{\mathrm{Re}}}{R}\frac{\partial \psi}{\partial z}+1 \qquad \text{at } z = 0 \qquad (18)$$

$$u \to 0; \quad v \to 0; \quad \theta \to 0; \quad \phi \to 0; \quad \psi \to 0\} \quad \text{as } z \to \infty \qquad (19)$$

The dimensionless boundary value problem defined by Eqns. (11)-(19) may further be simplified by deploying the following similarity relations (Bég et al. [50]) as follows:

$$\eta = z\,r^{-m}, \quad u = r^{1-2m} f'(\eta), \quad v = r^{1-2m} g(\eta), \quad w = -r^{-m}\big((2-m) f(\eta) - m\eta f'(\eta)\big),$$

$$\theta = \theta(\eta), \phi = \phi(\eta), \quad \psi = \psi(\eta) \qquad (20)$$

Substituting Eqn. (20) into Eqns. (11)-(17), wherein the continuity equation is automatically satisfied, results in the following form as:

Radial momentum

$$f''' + \frac{C_1}{C_2}(2-m) f f'' - \frac{C_1}{C_2}(1-2m)(f')^2 + \frac{C_1}{C_2} g^2 - \frac{1}{Da} f' = 0 \qquad (21)$$

Tangential (circumferential) momentum

$$g'' + \frac{C_1}{C_2}(2-m) f g' - \frac{C_1}{C_2}(2-2m) f' g - \frac{1}{Da} g = 0 \qquad (22)$$

Energy:

$$\theta'' + \frac{C_4}{C_3}\mathrm{Pr}(2-m) f \theta' = 0 \qquad (23)$$

Nanoparticle species:

$$\phi'' + \frac{C_4}{C_3}\mathrm{Pr}(2-m) f \phi' = 0 \qquad (24)$$

Micro-organism species:

$$\psi'' + Sb(2-m) f \psi' - Pe(\psi' \phi' + \psi \phi'') = 0 \qquad (25)$$

The conditions on the boundary as given in Eqns. (18) and (19) emerge as:

$$f'(0) = \frac{C_2}{C_1}\delta_u f''(0); \, g(0) = 1 + \frac{C_2}{C_1}\delta_v g'(0); \, f(0) = \frac{s}{Sc(2-m)}\phi'(0)$$

$$\theta(0) = 1 + \delta_T \theta'(0); \, \phi(0) = 1 + \delta_C \phi'(0); \, \psi(0) = 1 + \delta_n \psi'(0) \qquad \text{at } \eta = 0 \qquad (26)$$

$$f'(+\infty) \to 0; \quad g(+\infty) \to 0; \quad \theta(+\infty) \to 0; \quad \phi(+\infty) \to 0; \quad \psi(+\infty) \to 0 \quad \text{as} \quad \eta \to \infty \tag{27}$$

In Eqns. (21)-(27), the non-dimensional parameters featured are: radial stream function (f), circumferential stream function (g), temperature (θ), concentration (ϕ), motile microorganism density number (ψ), rotational Reynolds number $\left(\text{Re} = \dfrac{\Omega R^2}{v_f} \right)$, Darcy number $\left(Da = \dfrac{r \, \Omega K_0}{v_f} \right)$, Prandtl number $\left(\text{Pr} = \dfrac{v_f}{\alpha_f} \right)$, bioconvection Péclet number $\left(Pe = \dfrac{\tilde{b} \, W_c}{D_n} \right)$, Schmidt number $\left(Sc = \dfrac{v_f}{D} \right)$, bioconvection Schmidt number $\left(Sb = \dfrac{v_f}{D_n} \right)$, radial momentum slip $\left(\delta_u = \dfrac{(N_1)_0 \, v_f \, \sqrt{\text{Re}}}{R} \right)$, circumferential (tangential) momentum slip $\left(\delta_v = \dfrac{(N_2)_0 \, v \, \sqrt{\text{Re}}}{R} \right)$, thermal slip $\left(\delta_T = \dfrac{(D_1)_0 \, \sqrt{\text{Re}}}{R} \right)$, mass slip $\left(\delta_c = \dfrac{(E_1)_0 \, \sqrt{\text{Re}}}{R} \right)$, microorganism slip $\left(\delta_n = \dfrac{(F_1)_0 \, \sqrt{\text{Re}}}{R} \right)$, Stefan blowing parameter $\left(s = \dfrac{\Delta C}{1 - C_w} \right)$, density ratio $C_1 = \dfrac{\rho_{nf}}{\rho_f}$, dynamic viscosity ratio $C_2 = \dfrac{\mu_{nf}}{\mu_f}$, thermal conductivity ratio $C_3 = \dfrac{k_{nf}}{k_f}$, heat capacity ratio $C_4 = \dfrac{(\rho c_p)_{nf}}{(\rho c_p)_f}$. The following relations are used in the Tiwari-Das model to compute the nanofluid properties (Abu-Nada [51]).:

$$(\rho)_{nf} = (1 - Nc)\rho_f + Nc \, \rho_s \tag{28}$$

$$(\rho C_p)_{nf} = (1 - Nc)(\rho C_p)_f + Nc(\rho C_p)_s \tag{29}$$

$$\mu_{nf} = \frac{\mu_f}{(1 - Nc)^{2.5}} \tag{30}$$

$$K_{nf} = K_f \left(\frac{K_s + 2K_f - 2Nc(K_f - K_s)}{K_s + 2K_f + Nc(K_f - K_s)} \right) \tag{31}$$

Here Nc denotes the volume fraction (percentage doping) of nanoparticles, $(\ )_s$ represents solid nanoparticles, $(\ )_{nf}$ denotes nanofluid and $(\ )_f$ stands for base fluid. **Table 1** provides the values which are considered in this article (Abu-Nada [51]).

Table-1: Thermo physical properties.

Property	Pure water	Ag	Cu	Diamond	SiO₂	TiO₂
ρ (kg/m²)	997.1	10500	8933	3510	2200	4250
μ (Nm/s)	0.001	-	-	-	-	-
k (W/mK)	0.613	429	400	1000	1.2	8.5938
C_p (kJ/kgK)	4179	235	385	497.26	703	686.2
β (1/K)	207.10^{-6}	18.10^{-6}	17.10^{-6}	$1.0.10^{-6}$	$5.5.10^{-6}$	$0.17.10^{-6}$

Numerical values of the nanoparticle property ratio constants (C_1, C_2, C_3, C_4) for the five different nanofluids considered i.e. *copper-water, silver-water, diamond-water, silicon oxide-water and titanium oxide-water* are given in **Table 2**.

Table-2: Constants used in Tiwari-Das model for the five nanofluids studied with volume fraction $(Nc = 0.01)$

Nanofluid	C_1	C_2	C_3	C_4
Copper-water	1.07959	1.02544	1.03016	0.998254
Silver-water	1.09531	1.02544	1.03017	0.995922
Diamond-water	1.0252	1.02544	1.03025	1.00253
Silicon oxide	1.01206	1.02544	1.00728	1.00771
Titanium oxide	1.03262	1.02544	1.02478	1.00729

Table-3: Constants used in Tiwari-Das model for the copper-water nanofluid with different volume fractions (Nc)

Nc	C_1	C_2	C_3	C_4
0 (pure water)	1.0	1.0	1.0	1.0
0.01	1.07959	1.02544	1.03016	0.998254
0.05	1.39795	1.13682	1.15713	0.991268
0.1	1.7959	1.30135	1.33164	0.982537

The positive values of Stefan blowing parameter, s imply that the mass flux moves from the disk to the free stream and the opposite trend is attained for negative values of s (see- Bég *et al*. [50]). Key engineering design quantities of relevance to coating processes, are the gradients of the transport functions at the disk surface (wall) and these are defined mathematically as follows:

Radial local skin friction along $\bar{r}$ -direction

$$\left(C_{f\bar{r}} = \frac{\tau_{\bar{r}}}{\rho_f \; \bar{u}^2} \right), \tag{32}$$

Tangential local skin friction along θ -direction

$$\left(C_{f\theta} = \frac{\tau_{\theta}}{\rho_f \; \bar{v}^2} \right) \tag{33}$$

Nusselt number

$$\left(Nu_{\bar{r}} = \frac{\bar{r} \; q_w}{k_f \left(T_w - T_\infty \right)} \right) \tag{34}$$

Nanoparticle species Sherwood number:

$$\left(Sh_{\bar{r}} = \frac{\bar{r} \; q_m}{D \left(C_w - C_\infty \right)} \right) \tag{35}$$

Wall motile microorganism number density gradient:

$$\left(Nn_{\bar{r}} = \frac{\bar{r} \; q_n}{D_n \; n_w} \right) \tag{36}$$

Here the dimensional radial shear stress, dimensional tangential stress, surface heat flux, surface nanoparticle mass flux and surface micro-organism species mass flux are defined respectively as:

$$\tau_{\bar{r}} = \left(\frac{\partial \bar{u}}{\partial \bar{z}} + \frac{\partial \bar{w}}{\partial \bar{r}} \right)_{\bar{z}=0}, \quad \tau_{\theta} = \left(\frac{\partial \bar{v}}{\partial \bar{z}} + \frac{\partial \bar{w}}{\partial \bar{r}} \right)_{\bar{z}=0}, \quad q_w = - k_{nf} \left(\frac{\partial T}{\partial \bar{z}} \right)_{\bar{z}=0},$$

$$q_m = - D \left(\frac{\partial C}{\partial \bar{z}} \right)_{\bar{z}=0}, \quad q_n = - D_n \left(\frac{\partial n}{\partial \bar{z}} \right)_{\bar{z}=0}. \tag{37}$$

The appropriate expressions required in terms of the similarity variables for the quantities in Eqns. (32)-(36) by virtue of the transformations in Eqn. (20) may then be shown to take the form:

$$\sqrt{Re_{\bar{r}}} \ \ C_{f\bar{r}} = \frac{C_2}{C_1} f''(0), \sqrt{Re_{\bar{r}}} \ \ C_{f\theta} = \frac{C_2}{C_1} g'(0), \ \frac{1}{\sqrt{Re_{\bar{r}}}} Nu_{\bar{r}} = -\frac{C_3}{C_4} \theta'(0),$$

$$\frac{1}{\sqrt{Re_{\bar{r}}}} Sh_{\bar{r}} = -\phi'(0), \ \ \frac{1}{\sqrt{Re_{\bar{r}}}} Nn_{\bar{r}} = -\psi'(0) \tag{38}$$

Here $Re_{\bar{r}} = \frac{\Omega R^2}{v_f \ r^{2(m-1)}}$ is the *local* rotational Reynolds number. Note in actual computations

presented later, the quantities used are $f''(0), g'(0), -\theta'(0), -\phi'(0)$ and $-\psi'(0)$.

3. Computational solution with MATLAB BVP4C and validation

The dimensionless 11th order non-linear ordinary differential BVP (boundary value problem) defined by Eqns. (21)-(25) with conditions on the boundary (26, 27) may be solved with a variety of numerical methods. Here we adopt the MATLAB bvp4c routine Bég et al. [49]. The BVP solver bvp4c tool in MATLAB is very efficient at solving nonlinear coupled higher order differential equation systems.

To verify the MATLAB code, a comparison with the earlier Chebychev collocation solutions of Bég *et al*. [50] has been conducted and is shown in **Table 4,** for for $f''(0)$ and $g'(0)$. When *Nt=Nb=0, Le = Pr =1.0, m = −0.5, Da = 10.0, Pe=Sb=1.0,* $\delta_u = 0.0, \delta_v = \delta_\theta = \delta_c = \delta_n = 0.1$, in Bég *et al*. [49] and *Nc=0*, $C_1 = C_2 = C_3 = C_4 = 1$, *m = −0.5, Da = 10.0, Sc = 1, Pe=Sb =1.0,* $\delta_u = 0.0, \delta_v = \delta_\theta = \delta_c = \delta_n = 0.1$ is prescribed in the *present model*, the resulting equations and border conditions become identical and correspond to a pure fluid (absence of nanoscale effects). Also, a comparison with the solutions of Chen *et al*. [52] is conducted Generally, very good correlation is obtained, verifying the efficiency and reliability of the present MATLAB bvp4c methodology.

Table 4:Validation of MATLAB solutions with Chebyshev collocation solutions of Bég *et al*.[50] for $\delta_u = 0.0, \delta_v = \delta_\theta = \delta_c = \delta_n = 0.1$ and Chen *et al*. [52].

m = -0.5 (n=2)	$f''(0)$	$g'(0)$
Chen *et al*. [52] (Runge-Kutta)	0.4639	–0.6677
Beg *et al*. [49] (CSCM)	0.4601	–0.6677
Present (MATLAB bvp4c)	0.4650	-0.66827

4. Further validation using ADM

To further validate the general model solutions obtained with MATLAB, a different approach is required which provides a much more rigorous verification than merely benchmarking with existing simpler cases from the literature. Therefore, the Adomian decomposition method (ADM) Adomian [53]) is implemented. ADM is a power-series based semi-analytical/numerical method which is extremely adaptive and has been enabled successfully in a rich variety of multi-physical fluid mechanics problems including smart bio-magnetic tribology [55], magnetic polymer reactive coating boundary layer flows [56] and hydrogen magnetic fuel cells [57]. Implementing ADM, we use the following operators Adomian [53]:

$$L_1 = \frac{d^3}{d\eta^3}(\ )\ \text{ and }\ L_2 = \frac{d^2}{d\eta^2}(\ ) \tag{39}$$

The associated inverse operators are:

$$L_1^{-1}(\ ) = \int_0^\eta \int_0^\eta \int_0^\eta (\ )\, d\eta\, d\eta\, d\eta\ \text{ and }\ L_2^{-1}(\ ) = \int_0^\eta \int_0^\eta (\ )\, d\eta\, d\eta \tag{40}$$

The unknown functions $f, g, \theta, \phi,$ and ψ are expanded as power series in the Adomian polynomials :

$$f(n) = \sum_{m=0}^\infty f_m,\quad g(n) = \sum_{m=0}^\infty g_m,\quad \theta(n) = \sum_{m=0}^\infty \theta_m,\quad \phi(n) = \sum_{m=0}^\infty \phi_m,\quad \psi(n) = \sum_{m=0}^\infty \psi_m \tag{41}$$

The exact solutions are therefore developed as:

$$f(n) = Lim \sum_{m=0}^\infty f_m,\quad g(n) = Lim \sum_{m=0}^\infty g_m,\quad \theta(n) = Lim \sum_{m=0}^\infty \theta_m,\quad \phi(n) = Lim \sum_{m=0}^\infty \phi_m,\quad \psi(n) = Lim \sum_{m=0}^\infty \psi_m \tag{42}$$

Further details are given in [55]-[57]. The comparisons for $f''(0), g'(0), \theta'(0), \phi'(0), \psi'(0)$ are given in **Table 5**. Excellent correlation is achieved for all variables for different slip parameters $(\delta_u, \delta_v, \delta_T, \delta_c,\ \delta_n)$ and Stefan parameter (s) between MATLAB bvp4c and ADM. Confidence in the MATLAB code is therefore again strongly demonstrated. All Tiwari-Das data for the nanofluids studied is taken from **Table 3**.

Table 5: MATLAB versus ADM solutions for $f''(0), g'(0), \theta'(0), \phi'(0), \psi'(0)$ with

$m = -0.5,\ Da = 2.0,\ \Pr = 6.8,\ Nc = 0.01,\ Sc = Pe = Sb = 1.0,\ \delta_u = \delta_v = \delta_\theta = \delta_c = \delta_n = 0.1$

(Note - copper-water nanofluid is considered unless otherwise indicated).

	$f''(0)$ MATLAB	$f''(0)$ ADM	$-g'(0)$ MATLAB	$-g'(0)$ ADM	$-\theta'(0)$ MATLAB	$-\theta'(0)$ ADM	$-\phi'(0)$ MATLAB	$-\phi'(0)$ ADM	$-\psi'(0)$ MATLAB	$-\psi'(0)$ ADM
$\delta_u = 0.5$										
S Copper-water $(Nc = 0.01)$										
-1	0.12909	0.12921	1.3531	1.3527	3.9862	3.9857	0.98075	0.98071	1.6948	1.6952
0	0.20357	0.20361	0.91892	0.91884	0.99822	0.99831	0.36049	0.36055	0.61587	0.61579
1	0.21815	0.21823	0.83369	0.83373	0.34455	0.34462	0.24609	0.24614	0.39239	0.39244
$\delta_v = 0.5$										
S Copper-water										
-1	0.11911	0.11921	0.79582	0.79578	3.3468	3.3472	0.75222	0.75230	1.3402	1.3411
0	0.19058	0.19062	0.60795	0.60799	0.69046	0.69051	0.26283	0.26288	0.4473	0.4479
1	0.20503	0.20507	0.5678	0.56774	0.21256	0.21259	0.18236	0.18239	0.28392	0.28387
$\delta_T = 0.5$										
S Copper-water										
-1	0.21452	0.21457	1.2562	1.2564	1.4951	1.4954	0.88286	0.88291	1.5446	1.5449
0	0.29553	0.29558	0.84291	0.84287	0.619	0.6188	0.31193	0.31196	0.53089	0.53094
1	0.30806	0.30812	0.7636	0.76358	0.23843	0.23847	0.21373	0.21377	0.33597	0.33601
$\delta_c = 0.5$										
S Copper-water										
-1	0.25504	0.25508	1.0532	1.0535	2.5622	2.5628	0.48644	0.48649	0.98582	0.98586
0	0.29553	0.29561	0.84291	0.84294	0.8227	0.82274	0.27733	0.27738	0.50601	0.50604
1	0.30743	0.30748	0.76803	0.76807	0.28682	0.28687	0.20124	0.20127	0.3353	0.33541
$\delta_n = 0.5$										
S Copper-water										
-1	0.21452	0.21458	1.2562	1.2564	3.7196	3.7192	0.88286	0.88292	0.95473	0.95477
0	0.29553	0.29557	0.84291	0.84296	0.8227	0.8223	0.31193	0.31198	0.4379	0.4384
1	0.30806	0.30809	0.7636	0.76358	0.26356	0.26351	0.21373	0.21377	0.29617	0.29622
Diamond $Nc=0.01$										
S										
-1	0.20641	0.20646	1.2184	1.2189	3.735	3.7354	0.88521	0.88519	1.5481	1.5484
0	0.28225	0.28229	0.82863	0.82866	0.8171	0.8167	0.30978	0.30983	0.52709	0.52712
1	0.29414	0.29418	0.75407	0.75411	0.25954	0.25961	0.21176	0.21181	0.33265	0.33268
SiO2										
S										
-1	0.2044	0.2046	1.2093	1.20933	3.8000	3.8043	0.88572	0.88574	1.5488	1.5482
0	0.279	0.2793	0.82514	0.82516	0.82537	0.82542	0.30921	0.30926	0.5261	0.52614
1	0.29072	0.29068	0.75172	0.75169	0.2564	0.25637	0.21125	0.21133	0.33179	0.33183
$Nc=0.0$ (pure water)										
S										

-1	0.20645	0.20647	1.2186	1.21856	3.7977	3.7982	0.8852	0.88514	1.5481	1.5483
0	0.28231	0.28227	0.82869	0.82873	0.82708	0.82711	0.30979	0.30980	0.52711	0.52714
1	0.2942	0.29421	0.75411	0.75415	0.25737	0.25734	0.21177	0.21183	0.33266	0.33272

5. Graphical results and discussion

Figures 2-11 present the graphical results obtained with MATLAB bvp4c. In all plots,

$m = -0.5, Da = 10.0,$ Pr $= 6.8, Nc = 0.01, Sc = Pe = Sb = 1.0,$ $\delta_u = \delta_v = \delta_\theta = \delta_c = \delta_n = 0.1$ unless

otherwise indicated. In **Figs. 3-11** only *copper-water nanofluid coating* is considered. All data has

been extracted from Zhang [1], Bég et al. [50] and Das et al. [58] and is consistent with actual

properties of bio-nano-coating systems.

Figure 2 illustrates the transport characteristics computed i.e.(a) f', (b) θ, (c) ϕ (d) ψ for

different *metallic and carbon nanoparticles* in water base fluid. In all cases a radial velocity

overshoot (fig. 2a) is computed near the disk surface. Profiles then decay asymptotically to the free

stream. Silicon oxide-water nanofluid is observed to produce maximum radial flow velocity,

followed by diamond, then titanium, then copper and finally silver. Carbon-based nanoparticles

(silicon oxide) therefore achieve the best radial flow acceleration although the other nanoparticles

also perform well. Fig. 2b demonstrates that the opposite behavior is computed for temperatures.

Silver-water nanofluid achieves the maximum temperature, followed by diamond, copper, titanium

oxide with the minimum temperature associated with silicon oxide. Therefore, while radial velocity

is optimized with carbon-based nanoparticles, the temperature field is optimized with metallic

nanoparticles i.e. silver, and this is attributable to the higher thermal conductivity of metals which

exerts a profound effect on thermal enhancement. Fig. 2c shows that copper-water nanofluid

produces the highest nanoparticle concentrations followed by silver, diamond, silicon oxide and

finally titanium oxide. Nanoparticle diffusion is therefore optimized with copper nanoparticles

although there is minor difference computed for each nanoparticle. In all cases the maximum

nanoparticle concentration is located at the disk surface, where agglomeration is highest, and

thereafter a progressive depletion is computed throughout the boundary layer regime transverse to

the disk surface i.e. with η-coordinate. As with all other distributions, smooth profiles are computed

in the free stream, confirming that a sufficiently large infinity boundary condition has been

prescribed in MATLAB bvp4c. A similar trend to nanoparticle concentration response is observed

with the motile micro-organism density number distributions in Fig. 2d. Again, copper nanoparticles

produce the best propulsion in the gyrotactic micro-organisms, and this is connected with the

modification in thermal conductivity and viscosity of the nanofluid which is assistive to swimming of

the micro-organisms in the nanofluid coating boundary layer domain. Titanium oxide achieves the

lowest micro-organism density number magnitudes. However again the profiles are very close, and

all nanoparticles produce a satisfactory performance.

Figure 3 visualize the influence of different *nanoparticle solid volume fractions, Nc* for Copper-water nanofluid coating on f', θ, ϕ, ψ. The Tiwari-Das property ratios are functions of Nc, as per the definitions given in Eqns. (28)-(31), appear in multiple terms in the radial momentum eqn. (21), viz, $+\dfrac{C_1}{C_2}(2-m)f f''$, $-\dfrac{C_1}{C_2}(1-2m)(f')^2$ and also the tangential coupling term i.e. $\dfrac{C_1}{C_2}g^2$. A strong depletion in radial velocity is observed with increasing Nc, since the viscosity of the nanofluid is increased with greater nanoparticle presence. This induces radial flow deceleration and increases momentum boundary layer thickness. There is also a slight displacement in peak velocity further from the disk surface with increasing volume fraction. Pure water therefore produces superior radial flow characteristics to copper nanoparticle-water. However, the primary objective of thermal enhancement is clearly achieved in Fig. 3b wherein a strong temperature elevation is induced with greater nanoparticle volume fractions. Thermal boundary layer thickness is therefore elevated, and this is beneficial to improved coating design as noted in [1]. The radial velocity-temperature coupling term in the energy equation (22) i.e. $+\dfrac{C_4}{C_3}\Pr(2-m)f\phi'$ clearly contribute directly to the thermal enhancement observed. A noticeable elevation is also generated in the nanoparticle concentration magnitudes (Fig. 3c), although the increment is less dramatic over the same range of volume fractions. The term $+\dfrac{C_4}{C_3}\Pr(2-m)f\phi'$ in Eqn. (23) again makes a direct contribution to the modification in nanoparticle species concentrations with greater volume fraction as experienced via the thermal conductivity ratio $C_3=\dfrac{k_{nf}}{k_f}$ and heat capacity ratio $C_4=\dfrac{(\rho c_p)_{nf}}{(\rho c_p)_f}$. Nanoparticle species boundary layer thickness is therefore also increased, and mass diffusion of nanoparticles is boosted with greater doping. Fig. 3d demonstrates that propulsion of ψ is also accentuated with increasing nanoparticle volume fraction. Although there are no terms in the micro-organism density conservation eqn. (25), nevertheless the presence of multiple coupling terms i.e. $Sb(2-m)f\psi'$ and $-Pe(\psi'\phi'+\psi\phi'')$ link the micro-organism species field to f' and ϕ. This allows for the micro-organism diffusion to be influenced by Tiwari-Das nanofluid properties and manifests in the exacerbation of gyrotactic propulsion. A thicker micro-organism species boundary layer is therefore also produced with increasing copper nanoparticle volume fraction.

Figure 4 display the evolution in f', θ, ϕ, ψ for different Darcy number, *Da*. There is a distinct escalation in f' with increment in Da. $\left(Da=\dfrac{r\,\Omega K_0}{v_f}\right)$ features in both the Darcian impedance terms (which are linear drag force terms), in the radial momentum eqn. (21) i.e.

$-\dfrac{1}{Da}f'$ and the tangential momentum eqn. (22) i.e. $-\dfrac{1}{Da}f'$. They simulate the bulk matrix resistance of the solid fibers in the porous medium to the percolating nanofluid flow. As Darcy number is increased, the Darcian drag forces are depleted since permeability is increased and there is a progressive depletion in solid fibers impeding the nanofluid. This produces strong radial flow acceleration. The implication is that coating designers may suppress the radial flow with lower permeability media adjacent to the disk which may permit for more homogenous deposition of the film during spin coating. It is to be noted that the Darcy numbers deployed correspond to very sparsely packed porous media e.g. metallic foams, loosely packed biofilters etc, as noted by Vafai [45] and that strongly laminar flows only are considered for which higher order porous drag effects are not invoked. It is also judicious to note that Von Karman swirling flows generally produce maximum velocities near the disk surface as highlighted by Zandbergen and Dijkstra [11] and the velocity peaks near the wall (disk surface) confirm this trend in Fig. 4a. With increasing Darcy number, however there is a notable *depletion in temperatures* in the nanocoating regime (Fig. 4b). The systematic decrease in the presence of solid fibers in the porous medium with increment in permeability (higher Darcy number), reduce the thermal conduction in the regime. Although *forced thermal convection* is still present, the overall intensity of thermal diffusion is inhibited, and this results in a plummet in temperature magnitudes. Thermal boundary layer thickness is therefore elevated with greater Darcy number. Maximum temperatures always arise at the disk surface, in accordance with the boundary condition, and decay gradually to the free stream. Fig. 4c indicates that nanoparticle species concentration is also suppressed with increasing Darcy number. The cooling induced in the regime with greater permeability also influences the mass diffusion of the nanoparticles, via the coupling terms $\dfrac{C_4}{C_3}\Pr(2-m)f\theta'$ in eqn. (23) and $\dfrac{C_4}{C_3}\Pr(2-m)f\theta'$ in Eqn. (24). Although there is no direct coupling of the temperature and nanoparticle concentration fields, both are coupled to the radial velocity field which is strongly influenced by Darcy number. The radial acceleration induced with greater Darcy number (Fig. 4a) counteracts both thermal and nanoparticle diffusion. There is therefore a delicate interplay between all these flow characteristics. Fig. 4d also reveals that ψ magnitudes are also reduced with greater Darcy number. Again, since Darcian body forces are absent in the micro-organism species boundary layer Eqn. (25), the impact of the porous medium is experienced via the coupling of the micro-organism field with the radial velocity field as expressed in the term, $+Sb(2-m)f\psi'$. Propulsion of the gyrotactic micro-organisms is therefore inhibited with radial flow acceleration (due to higher Darcy number) and the micro-organism species boundary layer thickness in the coating is also reduced.

Figure 5 visualizes the evolution in f', θ, ϕ, ψ with axial coordinate (η) for different values of Stefan blowing parameter (s). A substantial r*adial flow deceleration is generated with negative values of s* whereas a significant *acceleration corresponds to positive values of s*. In the former case (suction, $s>0$), also known as reverse Stefan blowing, there is a boost in the mass flux from the potential flow to the disk surface. In the latter case, Stefan blowing $(s>0)$ mass flux from the disk to the potential flow external to the boundary layer regime is elevated. These situations are therefore more complex than conventional wall suction/injection boundary conditions computed with porous disk models (where the disk contains holes). In the present study the disk is in fact impervious i.e. solid. Momentum boundary layer thickness is therefore suppressed with positive Stefan blowing (radial flow acceleration) whereas it is accentuated with reverse Stefan blowing (suction produces deceleration). There is also a clear migration in the velocity peak away from the disk surface with Stefan blowing intensification. The peaks migrate closer to the disk surface with reverse Stefan blowing (suction). The conventional Von Karman swirling flow without Stefan blowing is retrieved for $s = 0$. Clearly this over-predicts the radial velocity compared to the suction (reverse Stefan blowing, $s < 0$) cases whereas it under-predicts the radial velocity relative to the Stefan blowing cases $(s>0)$. Backflow is never observed however for any values of s i.e. *flow reversal* is not computed in the boundary layer regime. The inclusion of Stefan blowing therefore exerts a substantial adjustment to the radial flow dynamics. A similar effect is computed on temperature field (Fig. 5b), nanoparticle species concentration (Fig. 5c) and also gyrotactic micro-organism density number (Fig. 5d). Intensification in Stefan blowing elevates θ i.e. heats the thermal boundary layer whereas reverse Stefan blowing cools the regime and decreases thermal boundary layer thickness. Similarly, nanoparticle concentration and micro-organism density number are boosted with increasing Stefan blowing $(s>0)$ whereas they are depleted with reverse Stefan blowing (s<0 i.e. suction).

Figure 6 visualizes the influence of *radial* momentum slip (δ_u) on f', θ, ϕ, ψ with transverse coordinate (η). A significant acceleration in f' is observed with increasing δ_u. A similar observation has been reported in Bég et al. [50]. However, the peak velocity is observed to be displaced closer to the disk surface with greater radial slip. Further from the disk surface, outside the primary influence of radial hydrodynamic wall slip, there is a weak radial deceleration which may be due to the re-distribution in momentum in the boundary layer. The absence of radial slip (δ_u) therefore produces an under-estimate in radial velocity near the disk surface and an over-estimate further from the disk surface. The inclusion of radial slip correctly predicts a higher near-wall radial velocity and a lower far field radial velocity deeper into the boundary layer away from the wall. Momentum boundary layer thickness is therefore appreciably modified with the inclusion of the

radial slip effect. Figs. 6b, 6c and 6d show that there is a strong depletion in temperature, nanoparticle concentration and motile micro-organism density, respectively, with increasing radial slip. Contrary to the radial velocity field (Fig. 6a), these trends are sustained throughout the boundary layer. The absence of radial slip in the mathematical model therefore over-predicts all these characteristics. Thermal boundary layer thickness, nanoparticle species boundary layer thickness and micro-organism species boundary layer thickness are all thinned with elevation in radial slip.

Figure 7 illustrates the evolution in f', θ, ϕ, ψ for different circumferential (tangential) momentum slip (δ_v). The opposite behavior is computed compared with the radial slip, in all graphs. A strong retardation is produced in the tangential flow (Fig. 7a) which is sustained for some distance from the disk surface. There is a slight switch further from the disk where a very weak acceleration arises with greater tangential slip parameter. The deceleration is probably due to the tangential momentum which is lost with a simultaneous boost in radial momentum. Momentum boundary layer thickness is therefore increased with greater tangential slip. Peak tangential velocity is also moved slightly *closer to the disk surface* with greater tangential slip. Temperature (Fig 7b), nanoparticle species concentration and micro-organism density number are however significantly increased with greater tangential slip. Therefore for the case where tangential slip is neglected ($\delta_v \rightarrow 0$), tangential velocity is a maximum (and momentum boundary layer thickness is minimal) whereas temperature, nanoparticle concentration and micro-organism density number are minimized with an associated maximum thickness in the boundary layers.

Figure 8 depicts the distributions for f', θ, ϕ, ψ with different thermal slip (δ_T). Negligible modification in radial velocity (Fig. 8a), nanoparticle concentration (Fig. 8c) and micro-organism slip (Fig. 8d) is observed with increasing thermal slip. However, a strong suppression in temperatures is computed with greater thermal slip. The jump in temperature at the disk surface produces a step change in temperature. This delays the penetration of heat from the disk surface to the boundary layer and decreases thermal diffusion. The effect is however progressively reduced with further distance into the boundary layer and achieves a maximum influence closer to the disk. Thermal boundary layer thickness is therefore depleted with higher thermal slip parameter values. However, the momentum, nanoparticle species and micro-organism species boundary layer thickness are not altered tangibly. The inclusion of thermal slip effectively permits a more accurate appraisal of near-wall temperature distribution which is critical in thermal manufacturing coating processes [7, 9]. Neglection of thermal slip ($\delta_T \rightarrow 0$), clearly leads to an *over-estimate* in temperatures.

Figure 9 presents the evolution in f', θ, ϕ, ψ with different nanoparticle mass slip (δ_c). As with all other slip parameters, δ_c arises in the wall (disk surface) boundary conditions i.e. Eqn. (26). A non-trivial modification in all flow characteristics is produced with nanoparticle mass slip

parameter. Fig. 9a shows that in the absence of this slip effect ($\delta_c = 0$), no effect is computed on the radial velocity (horizontal line). However, as δ_c increases, there is a marked elevation induced in radial velocity profiles which also assume inverted parabolic topologies. Maximum radial flow acceleration is therefore associated with the maximum nanoparticle slip value and hydrodynamic boundary layer thickness is reduced. For the case $\delta_c = 0$, the *step jump in temperature* is clearly computed (Fig. 9b). Increment in δ_c clearly enhances temperatures throughout the regime. A prominent elevation in nanoparticle concentration (Fig. 9c) and motile micro-organism density number (Fig. 9d) with increasing nanoparticle mass slip (δ_c) is also observed. Nanoparticle diffusion and gyrotactic micro-organism propulsion are therefore assisted strongly with greater nanoparticle mass slip effect. Effectively thermal, nanoparticle species and micro-organism boundary layer thicknesses are all accentuated with greater nanoparticle species effect. The incorporation of this slip effect is therefore very important in mathematical models for bio-nanocoating flows since it provides a much deeper insight into the actual response of the relevant variables to real wall effects encountered in coating synthesis operations.

Figure 10 illustrates the distributions for f', θ, ϕ, ψ with different micro-organism slip (δ_n). No significant change is computed in radial velocity, temperature or nanoparticle mass slip with increment in micro-organism slip (δ_n). However, a significant reduction in ψ accompanies an increment in δ_n. Micro-organism species boundary layer thickness in the coating is therefore depleted with greater micro-organism slip effect. Maximum micro-organism species boundary layer thickness accompanies the case where micro-organism slip is absent ($\delta_n = 0$). However, there is no tangible alteration in momentum, thermal or nanoparticle species boundary layer thicknesses.

Figure 11 displays the evolution in f'', g', θ', ϕ' and ψ' for different blowing parameter (s) and with different slip parameters. There is a substantial enhancement in f'' with positive values of Stefan blowing parameter, s whereas a depletion is computed with negative s as seen in Fig. 11a. The opposite trend is observed for tangential (circumferential) skin friction (Fig. 11b), Nusselt number (Fig. 11c), nanoparticle Sherwood number (Fig. 11d) and motile micro-organism density number gradient (Fig.11e). Increasing radial momentum slip reduces the f'' and increasing tangential slip suppresses the g'. θ', ϕ' and ψ' are all respectively reduced with increment in thermal slip, nanoparticle mass slip and micro-organism slip factors.
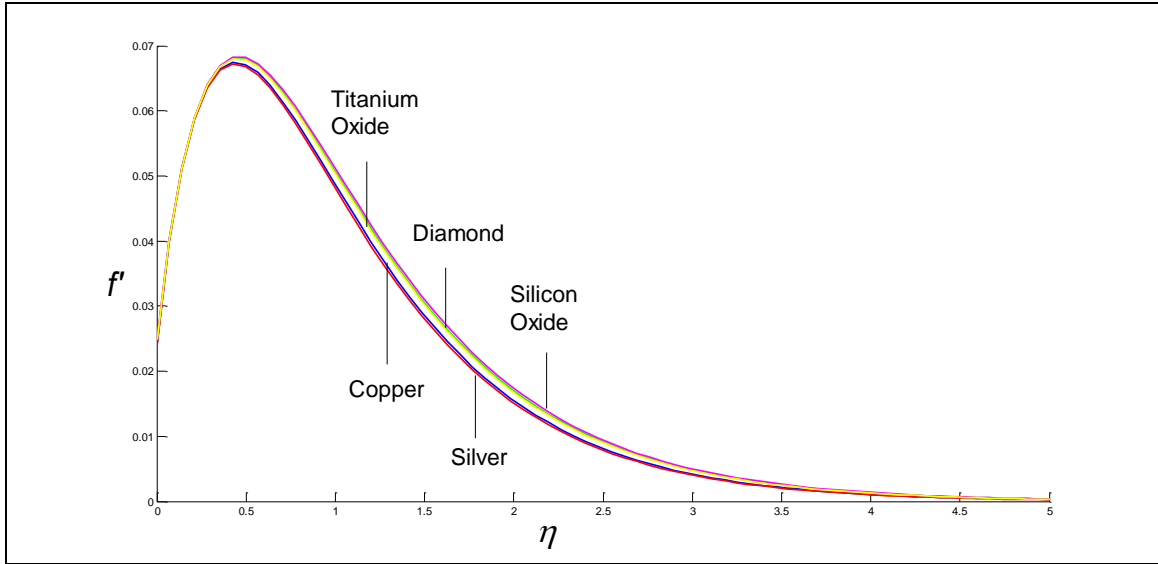
(a)
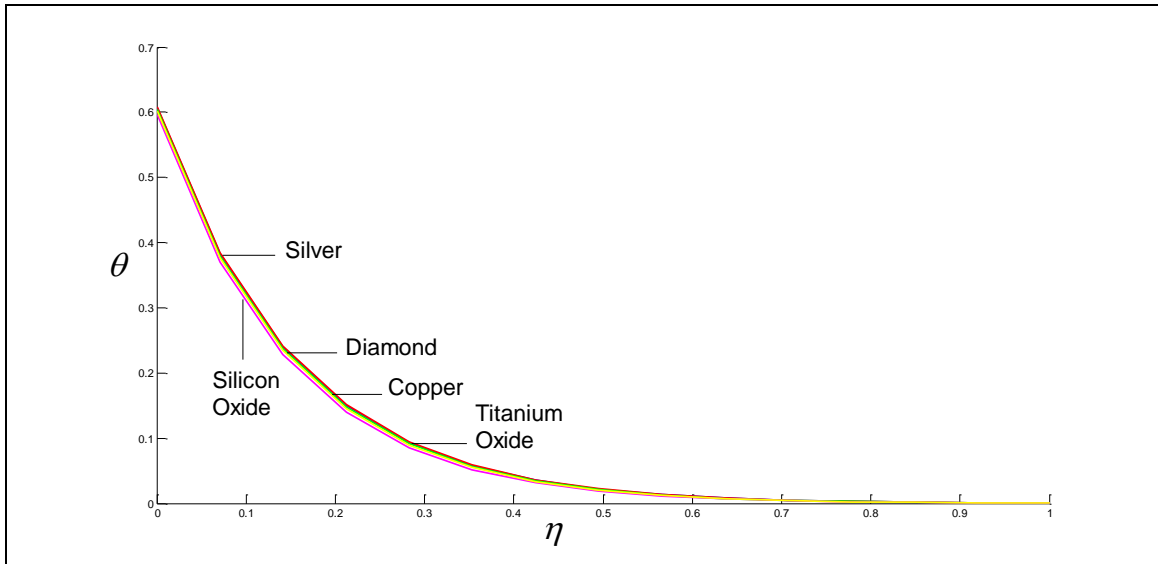
(b)
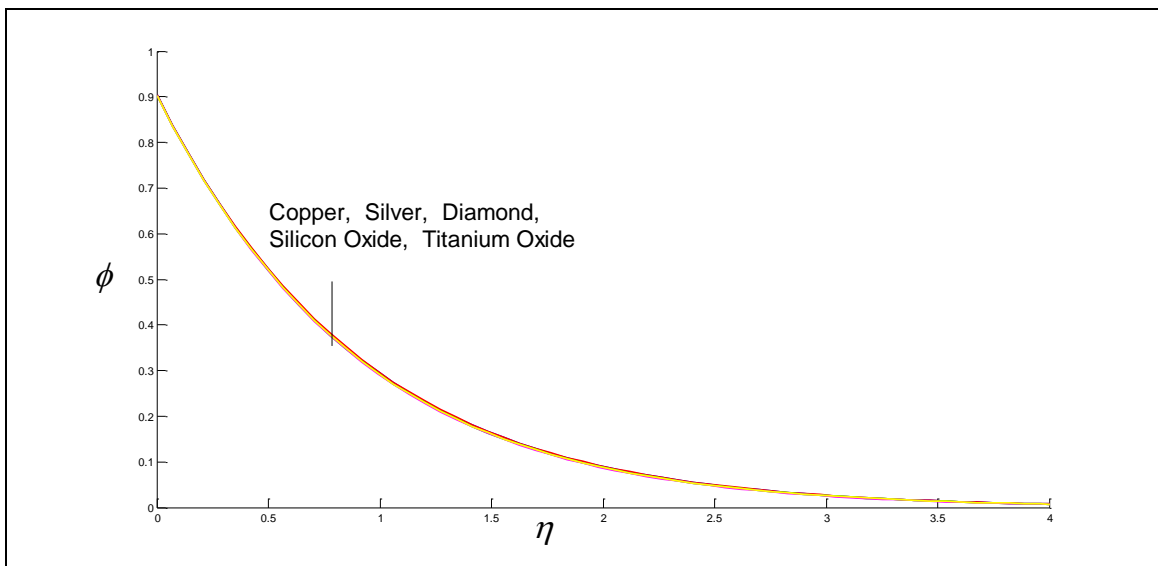
(c)
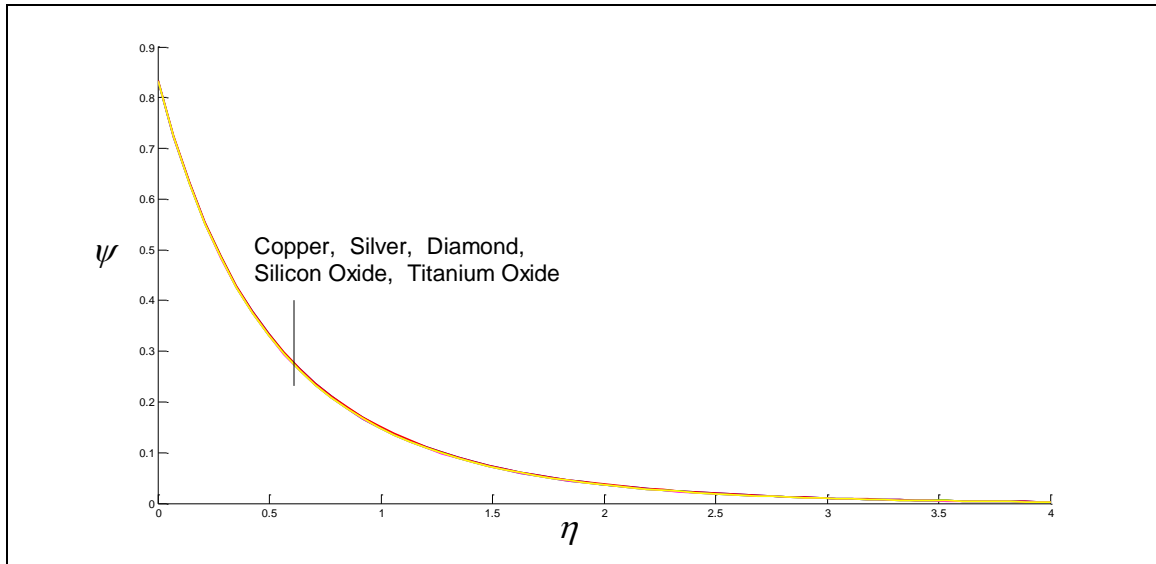
(d)

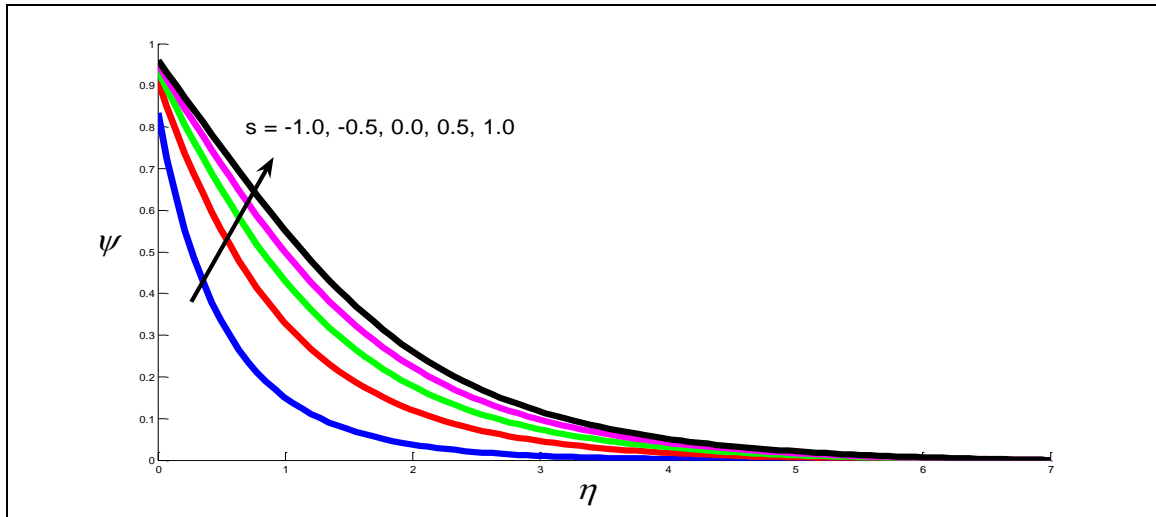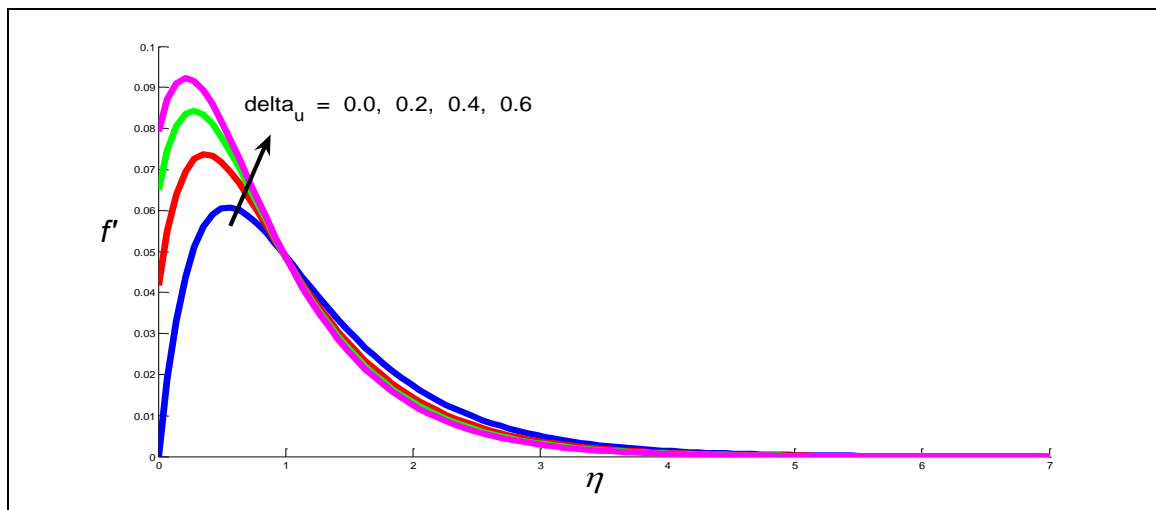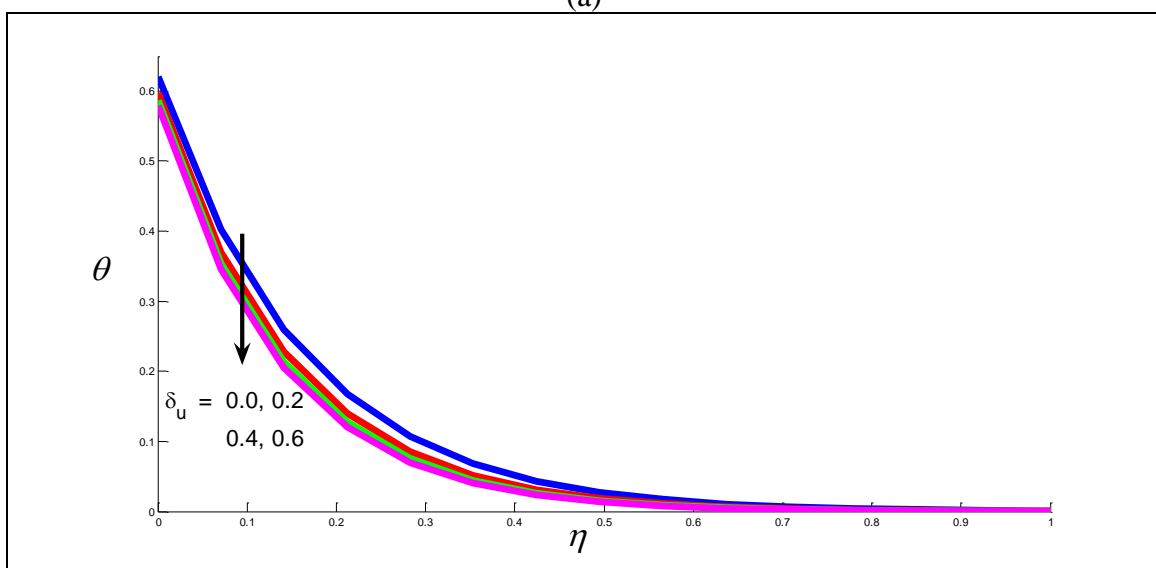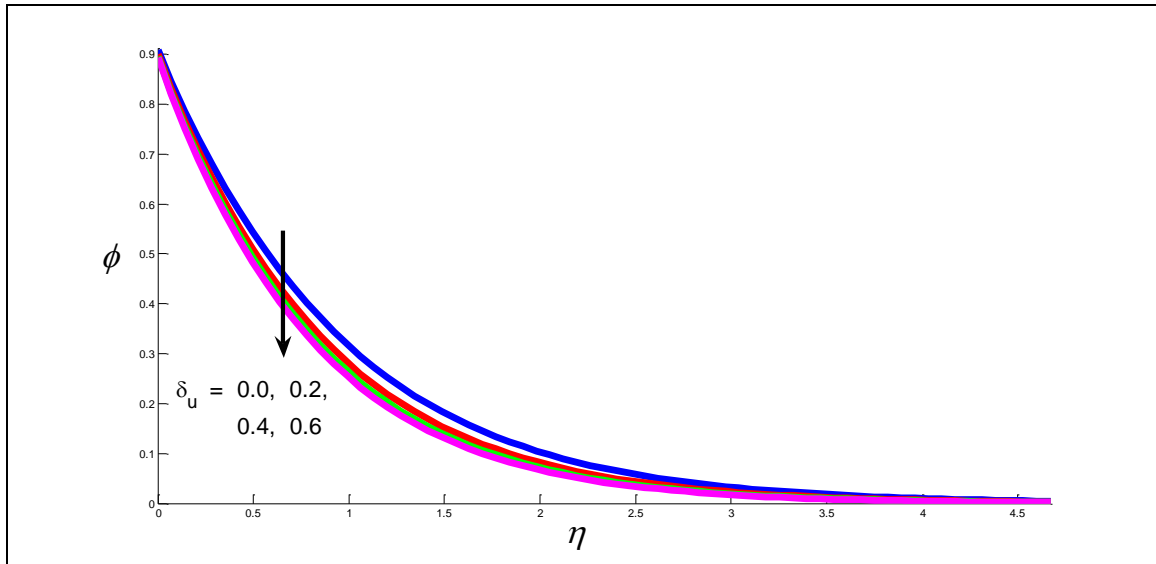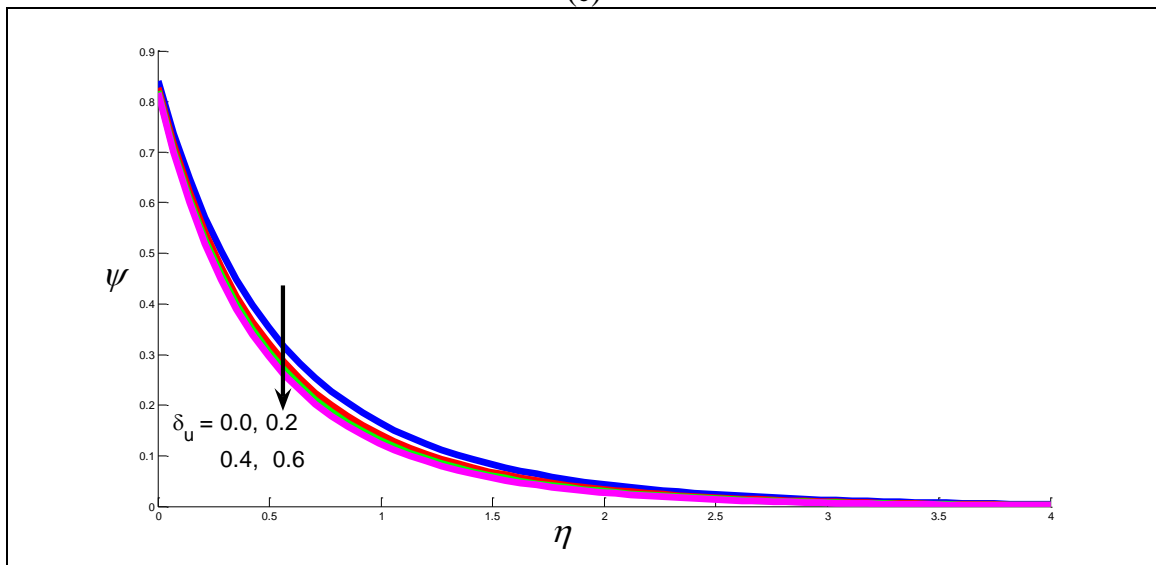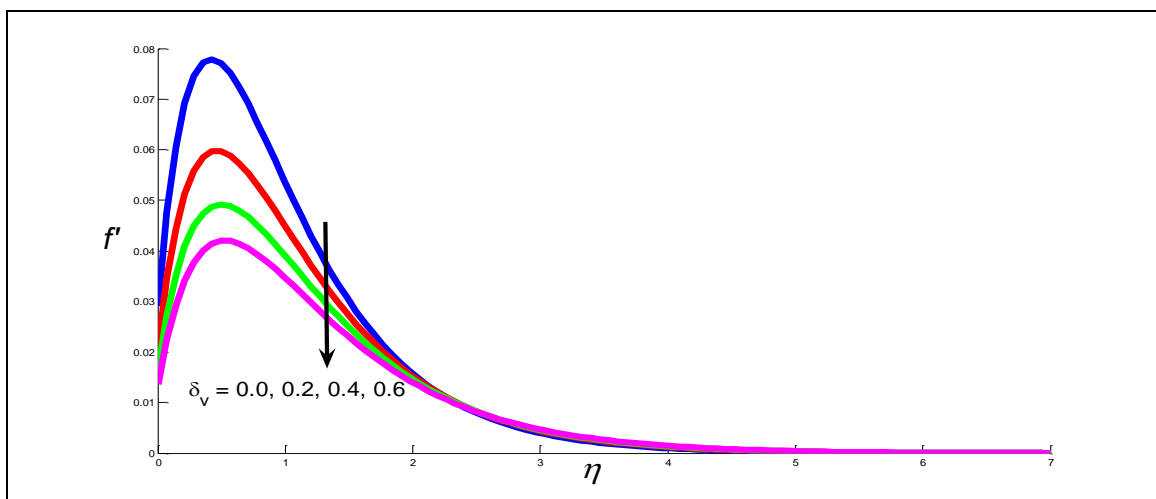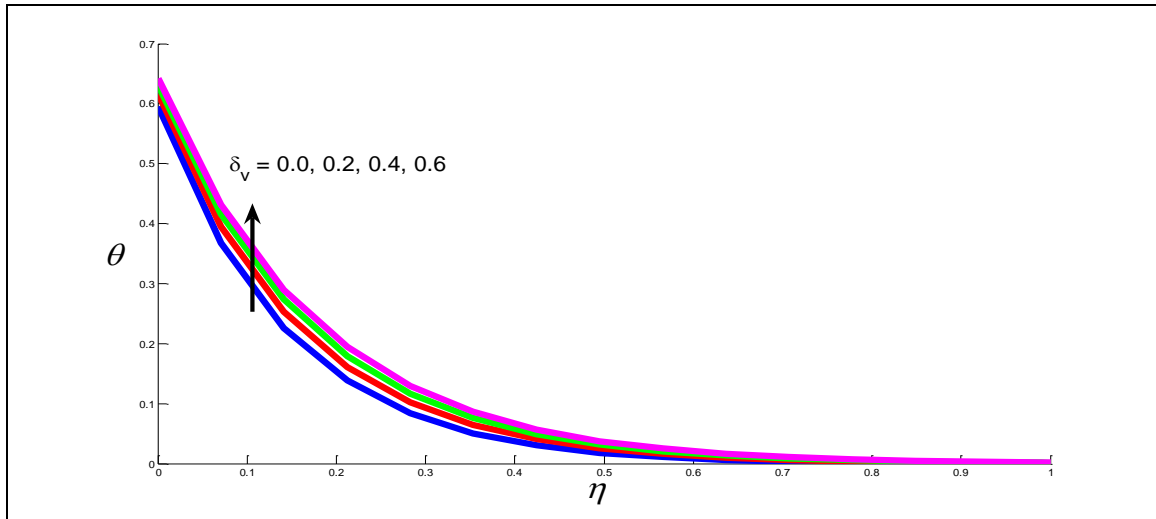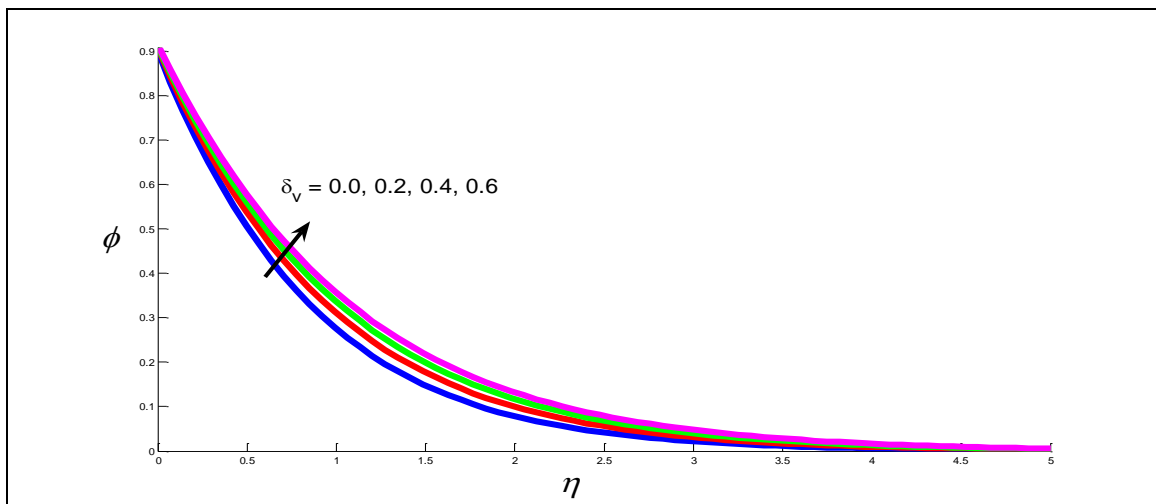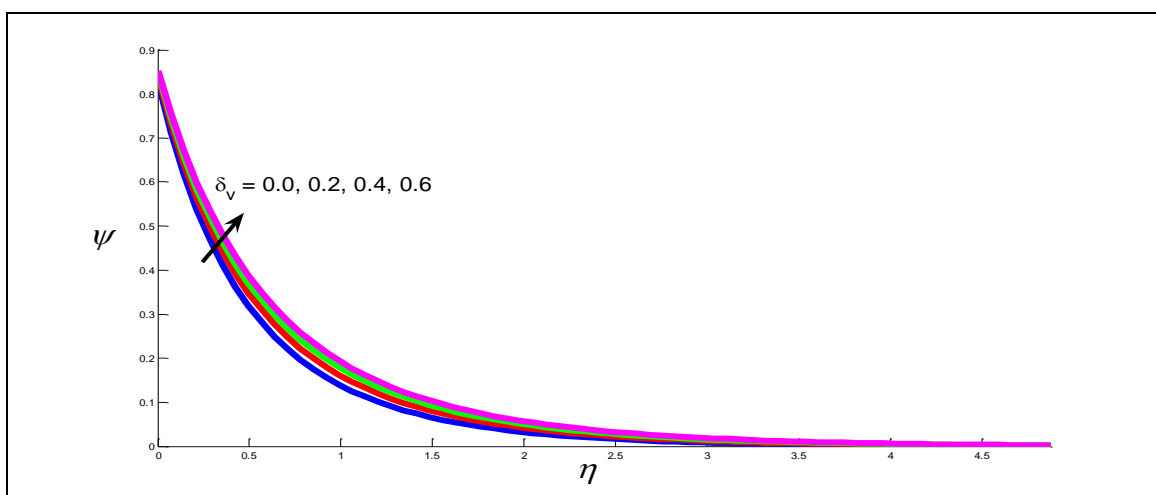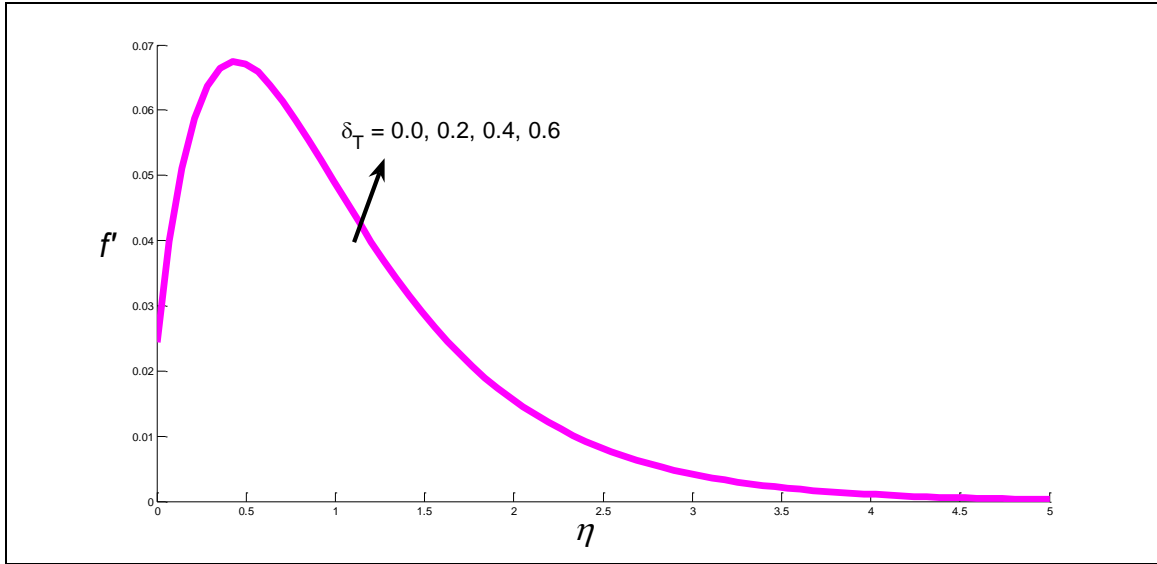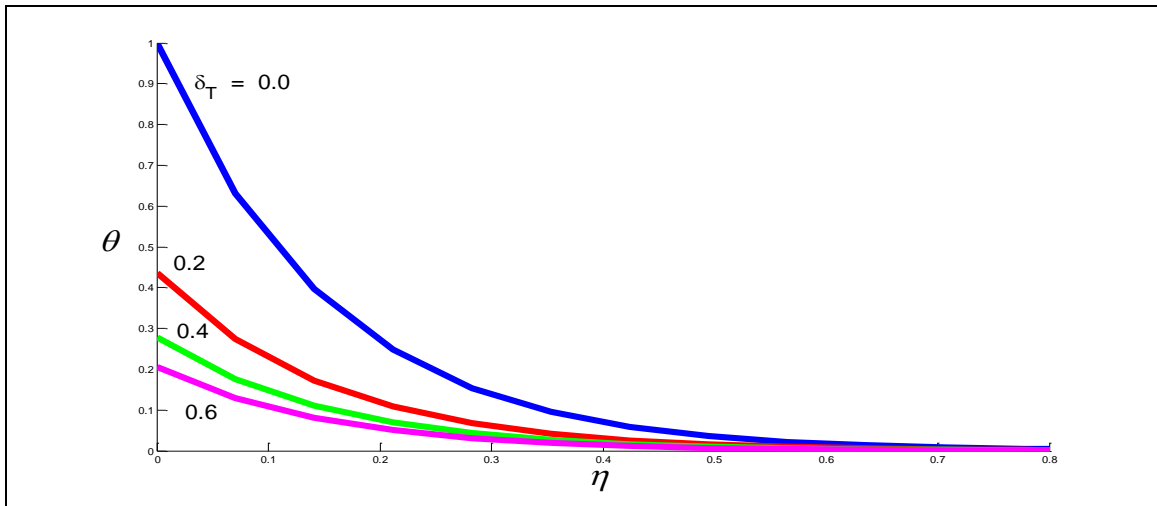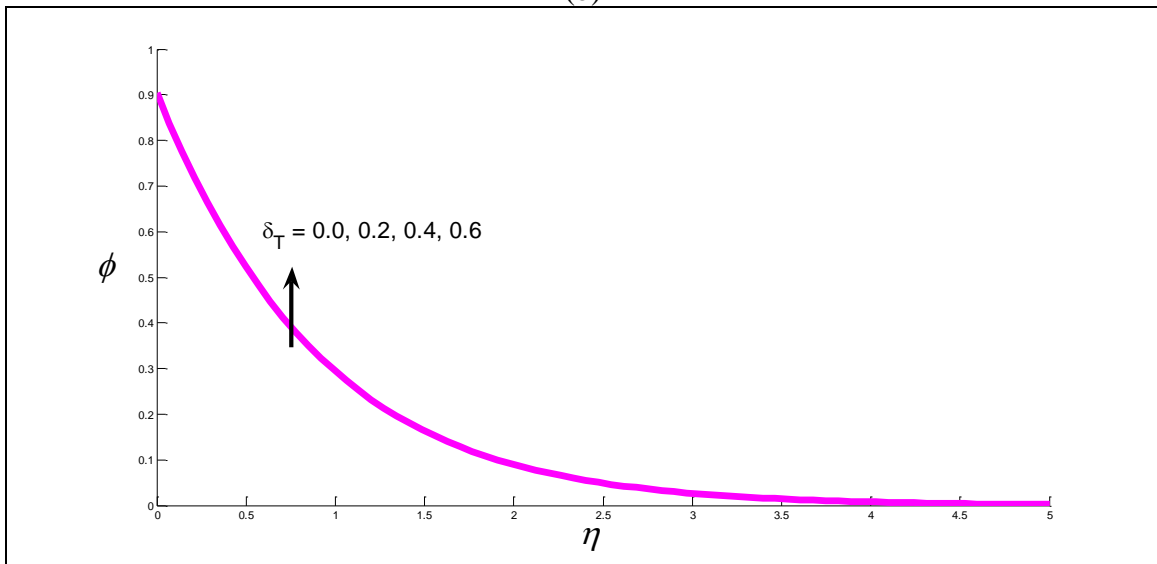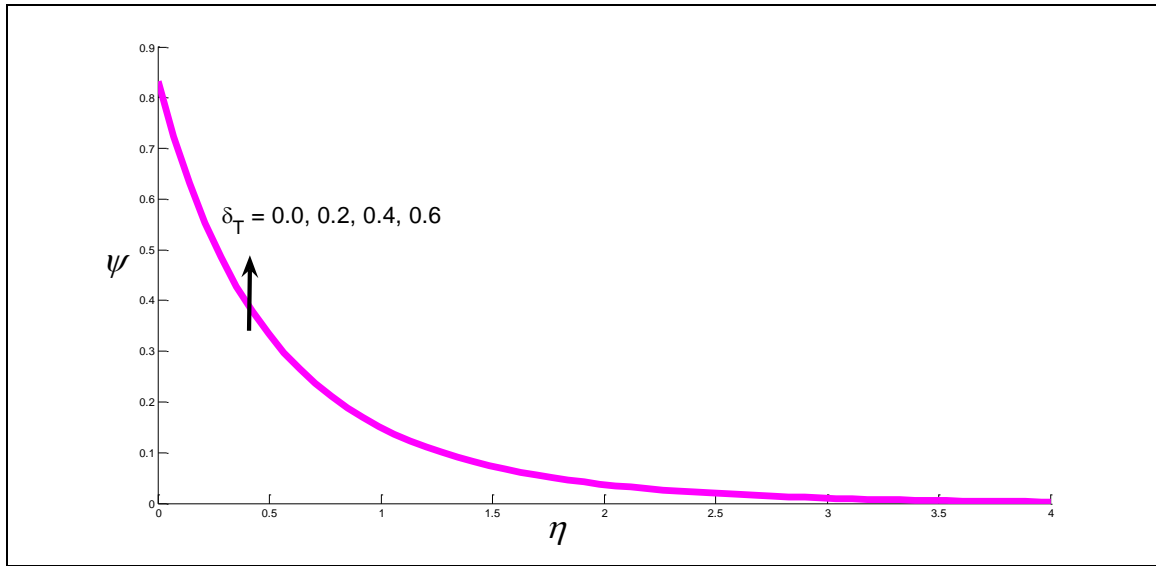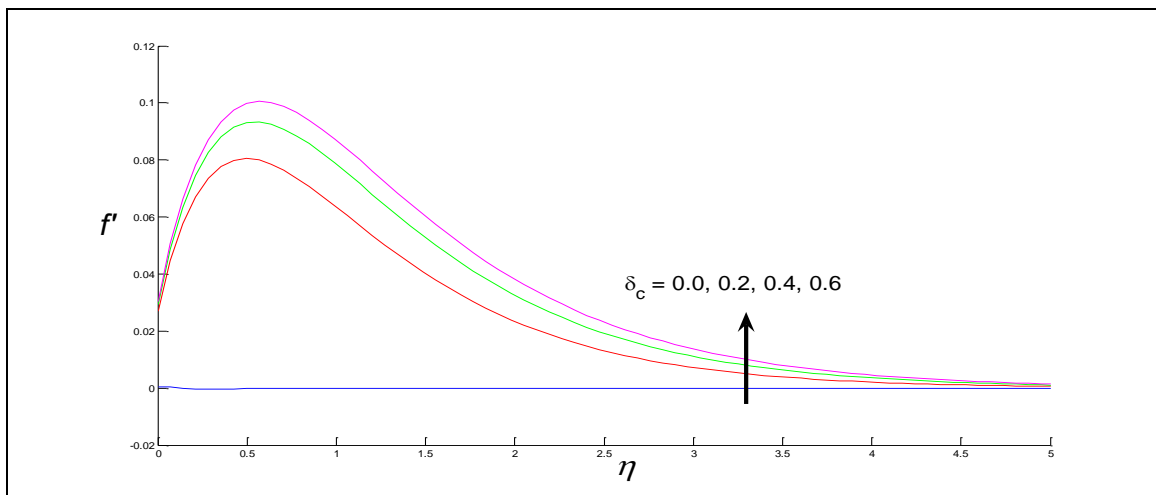**Figure 2.** a) Radial velocity b) temperature c) nanoparticle concentration and d) motile microorganism density number for different *metallic and carbon nanoparticles* in aqueous base fluid
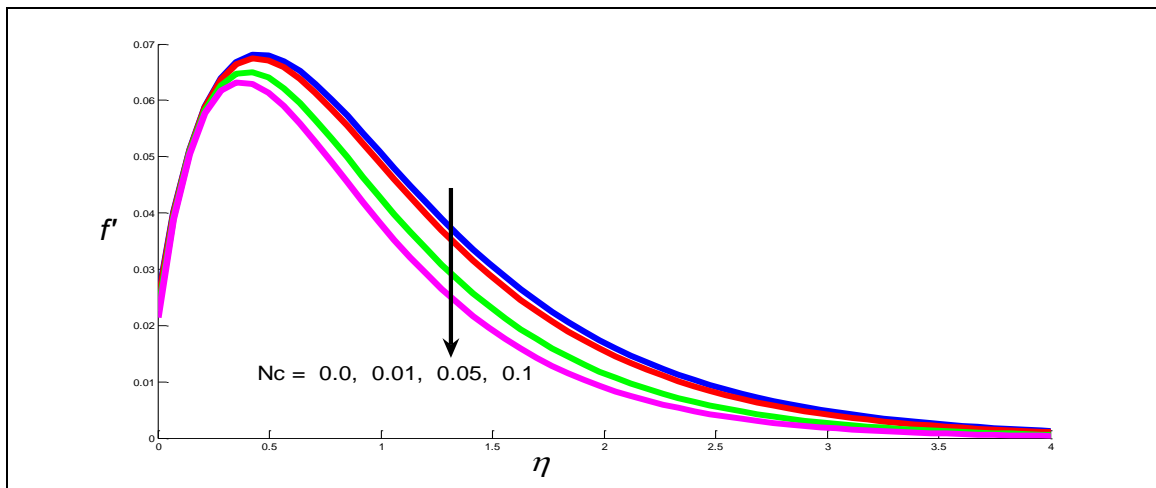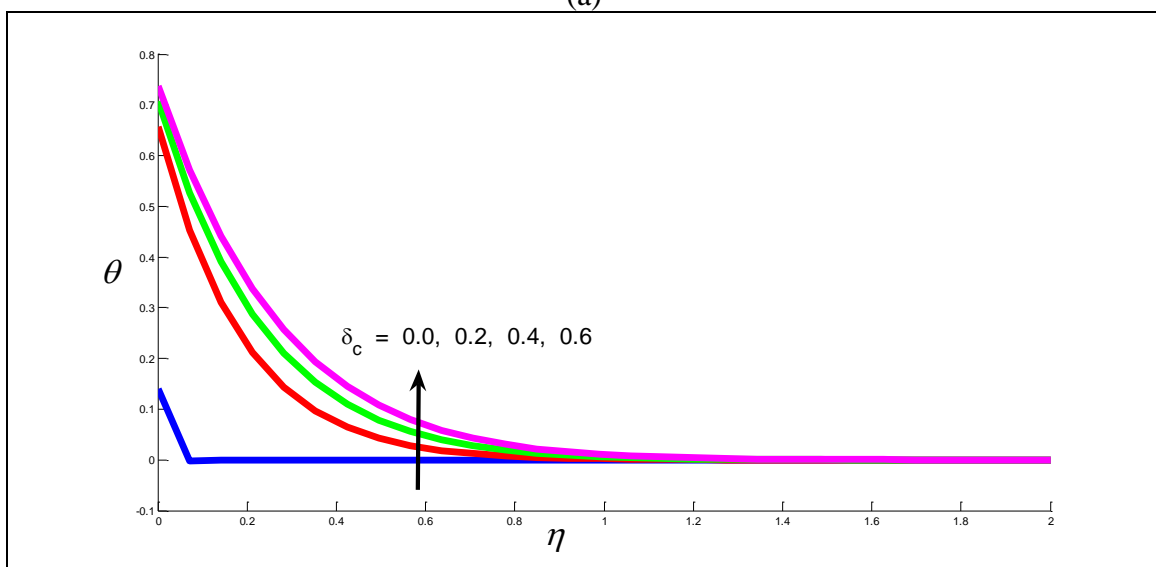

(a)
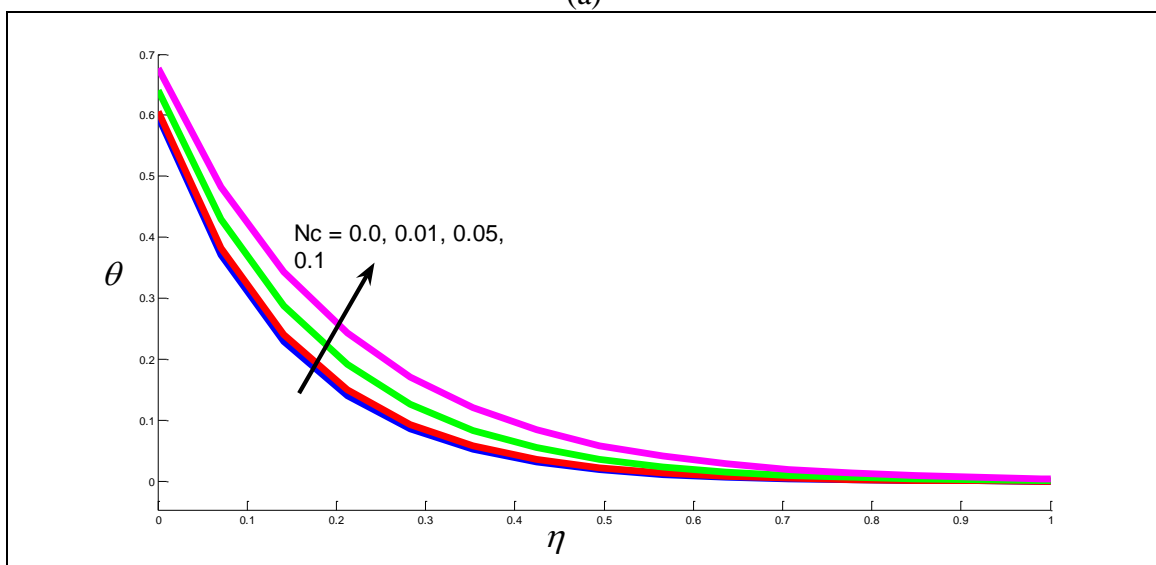
(b)
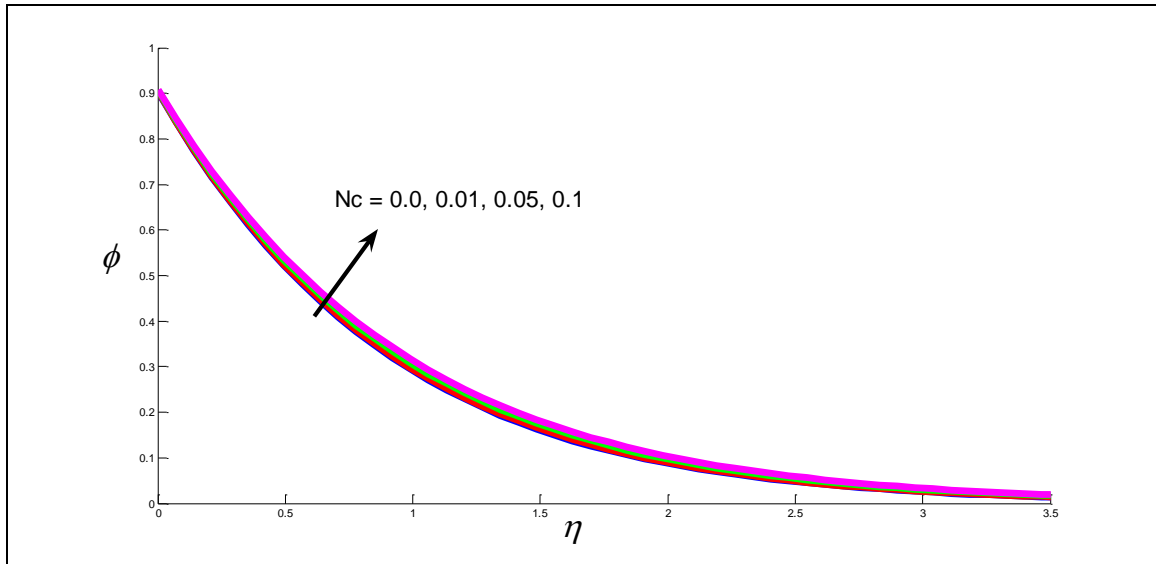
(c)
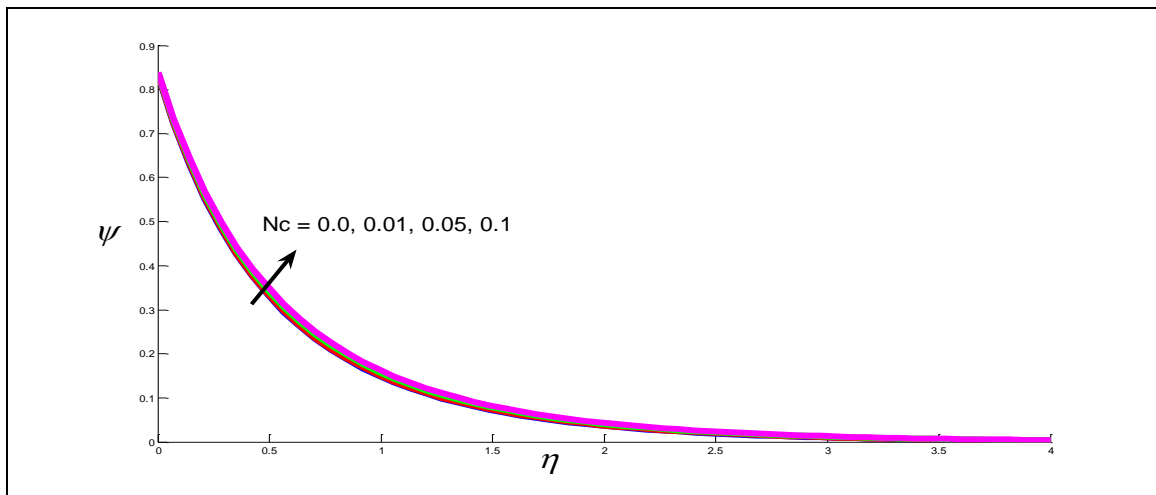
(d)

Figure 3. a) Radial velocity b) temperature c) nanoparticle concentration and d) motile microorganism density number for different *nanoparticle solid volume fraction, Nc* (Copper-water nanofluid coating)
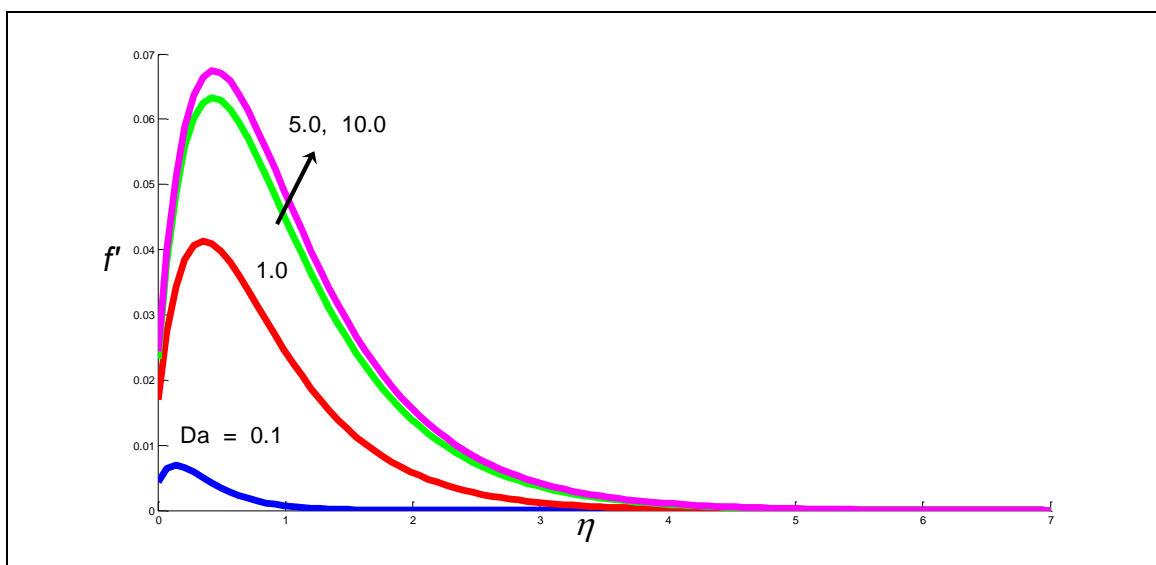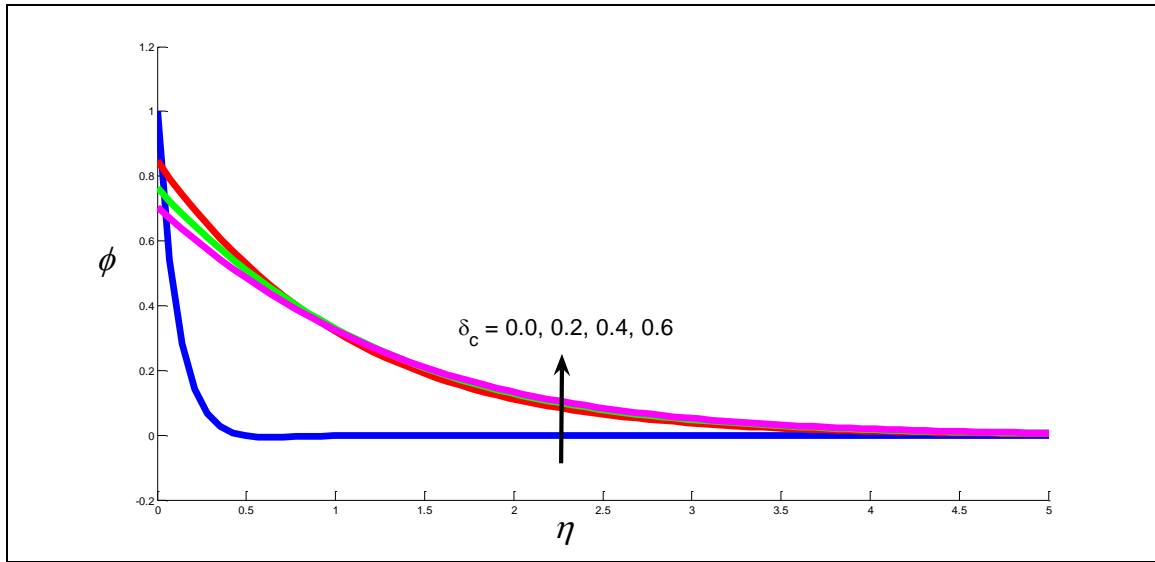

(a)
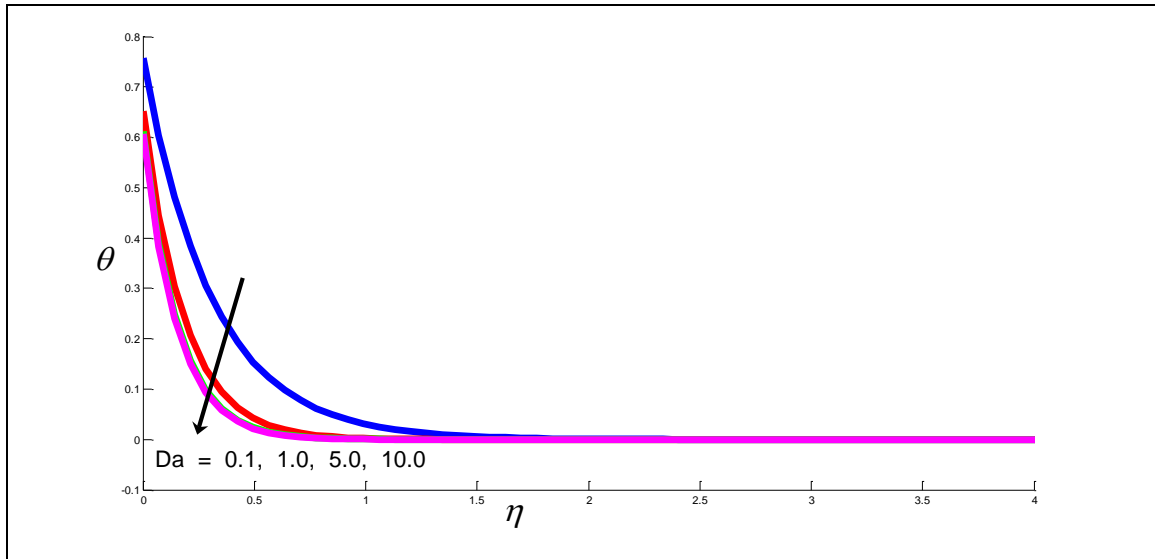
(b)
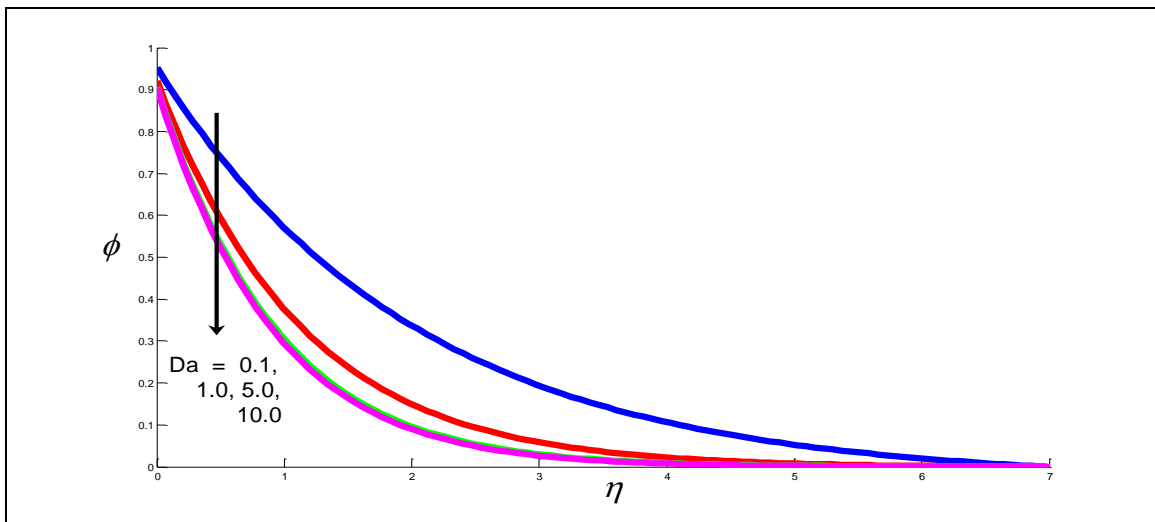
(c)
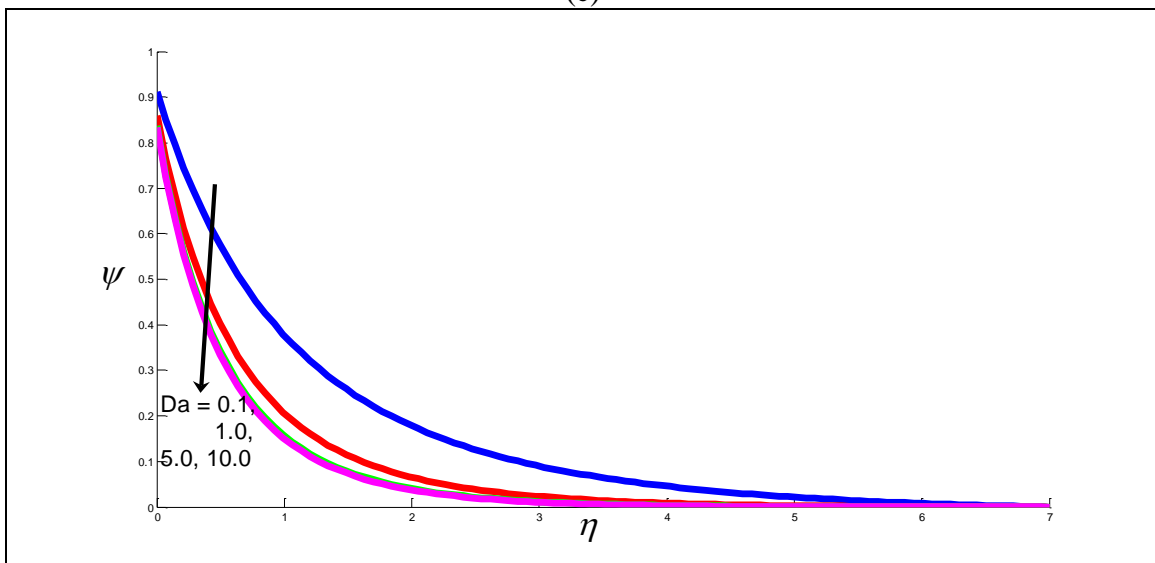
(d)

Figure 4. a) Radial velocity b) temperature c) nanoparticle concentration and d) motile microorganism density number for different Darcy number, Da.
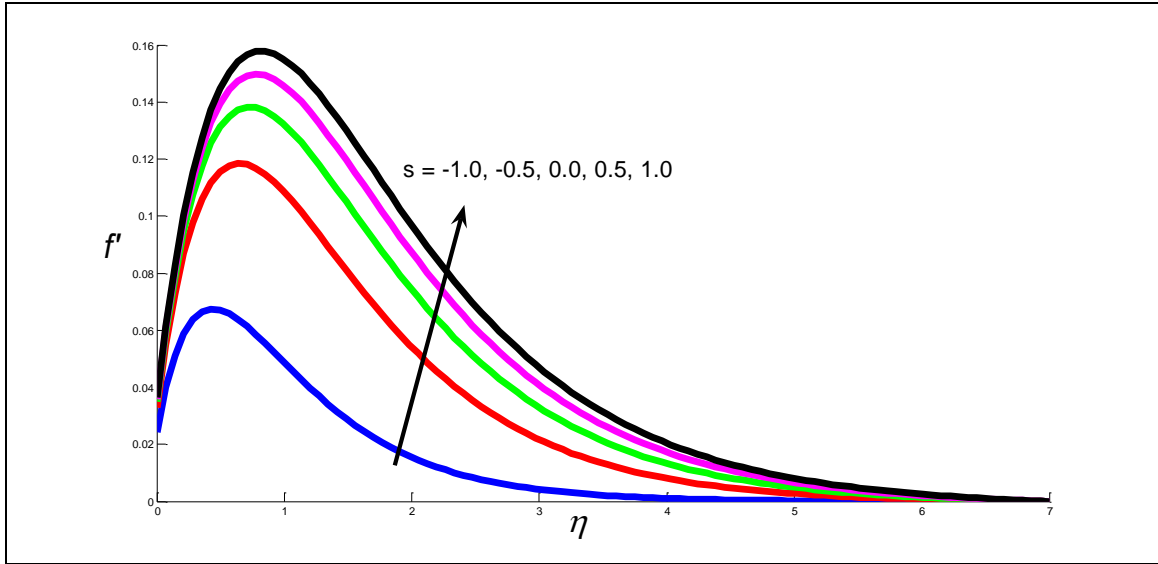
(a)
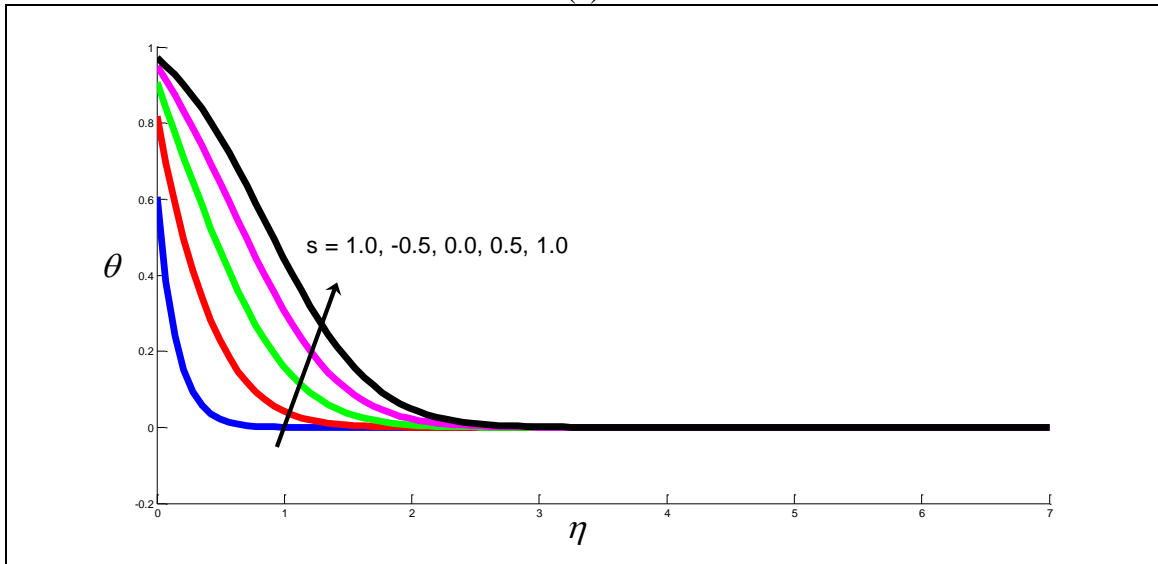
(b)
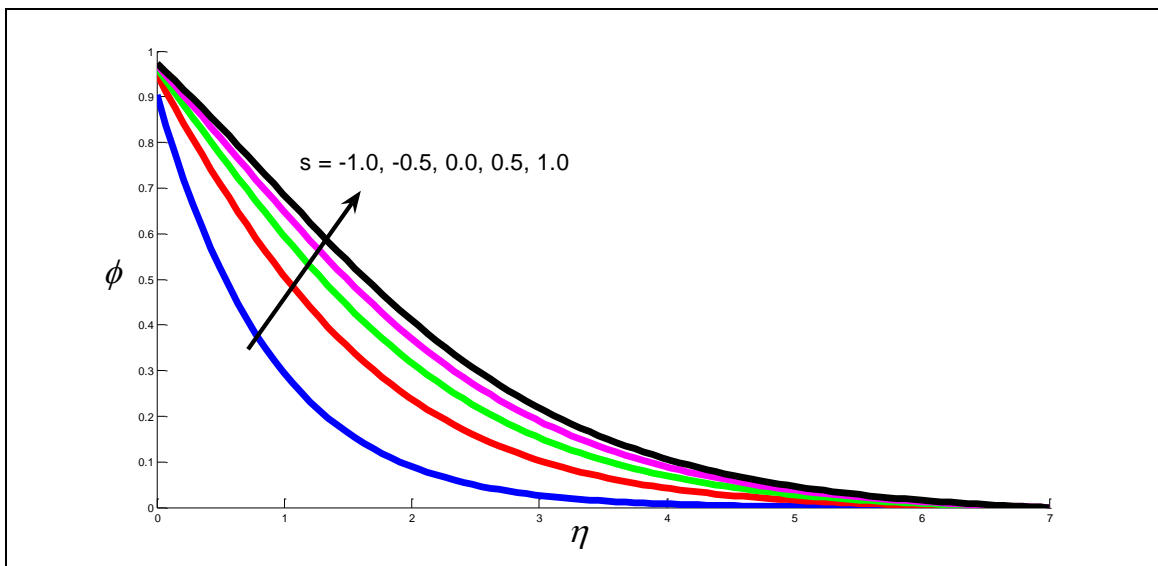
(c)

(d)

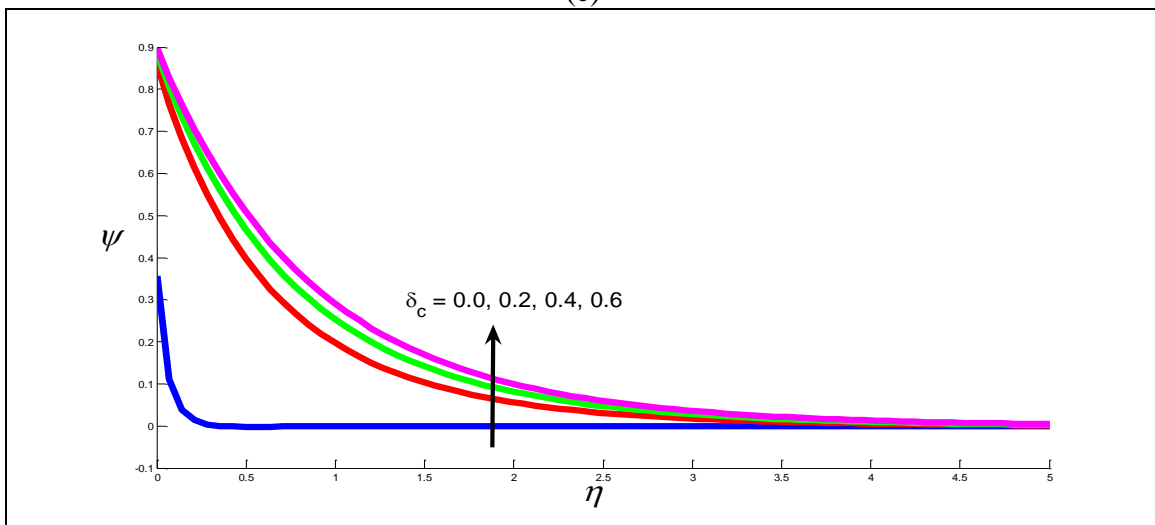**Figure 5.** a) Radial velocity b) temperature c) nanoparticle concentration and d) motile microorganism density number for different Stefan blowing parameter (*s*).

(a)

(b)

(c)

(d)

Figure 6. a) Radial velocity b) temperature c) nanoparticle concentration and d) motile micro-organism density number for different radial momentum slip (δ_u)
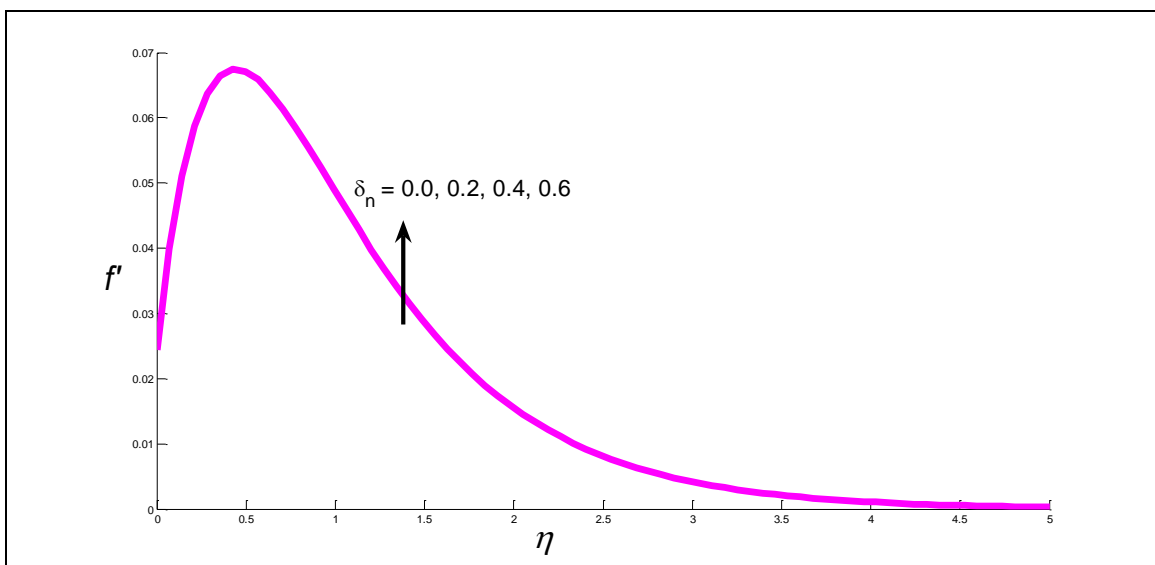

(a)

(b)

(c)

(d)

Figure 7. a) Radial velocity b) temperature c) nanoparticle concentration and d) motile micro-organism density number for different circumferential momentum slip (δ_v)

(a)

(b)

(c)

(d)

Figure 8. a) Radial velocity b) temperature c) nanoparticle concentration and d) motile micro-organism density number for different thermal slip (δ_T)
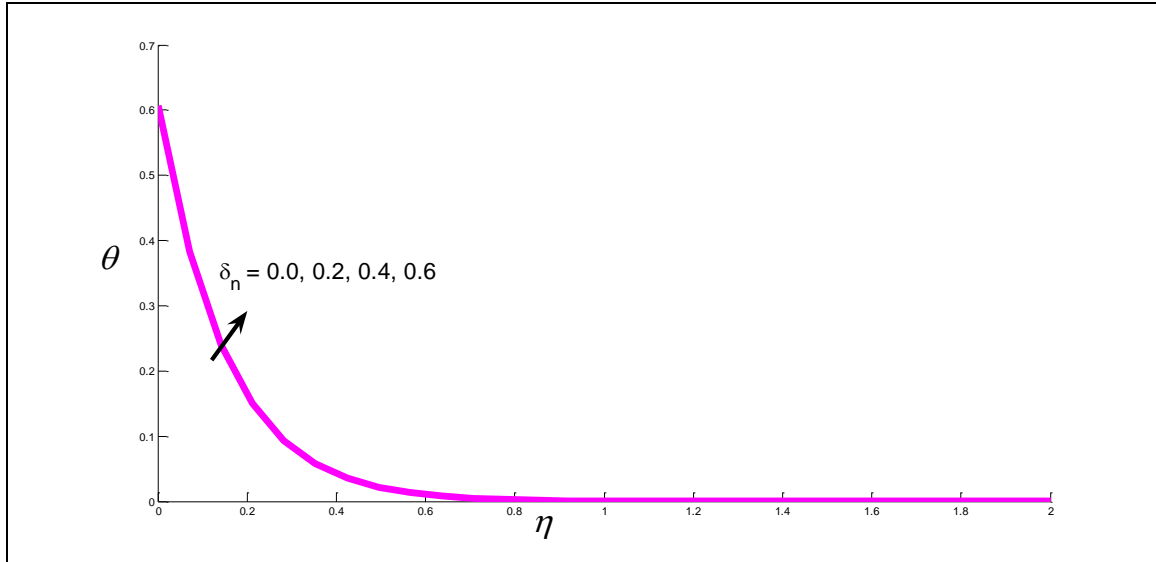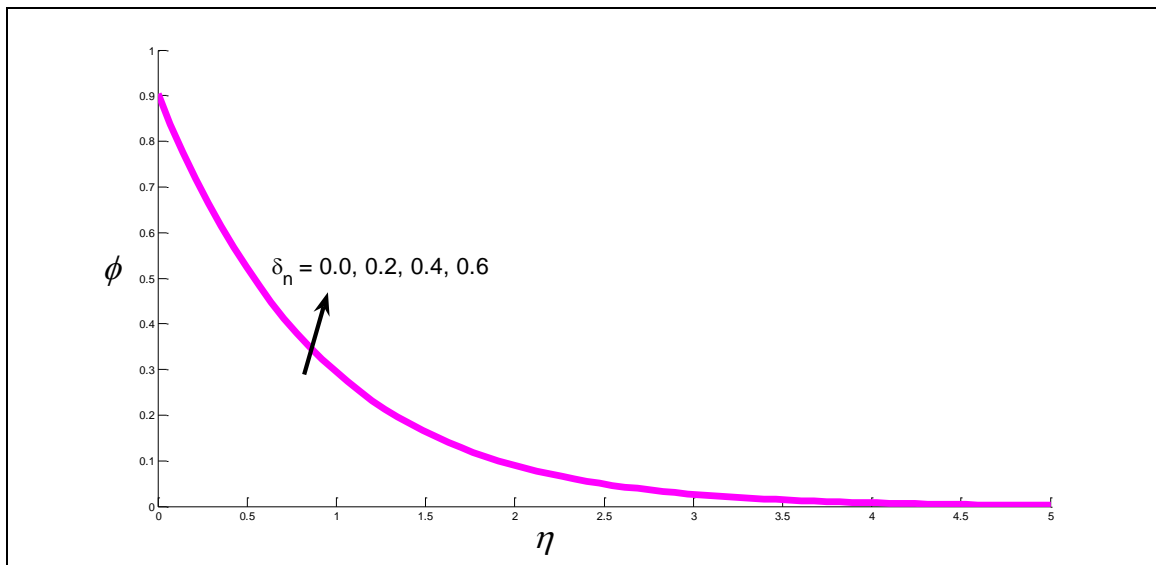

(a)

(b)

(c)

(d)

Figure 9. a) Radial velocity b) temperature c) nanoparticle concentration and d) motile micro-organism density number for different nanoparticle mass slip (δ_c)
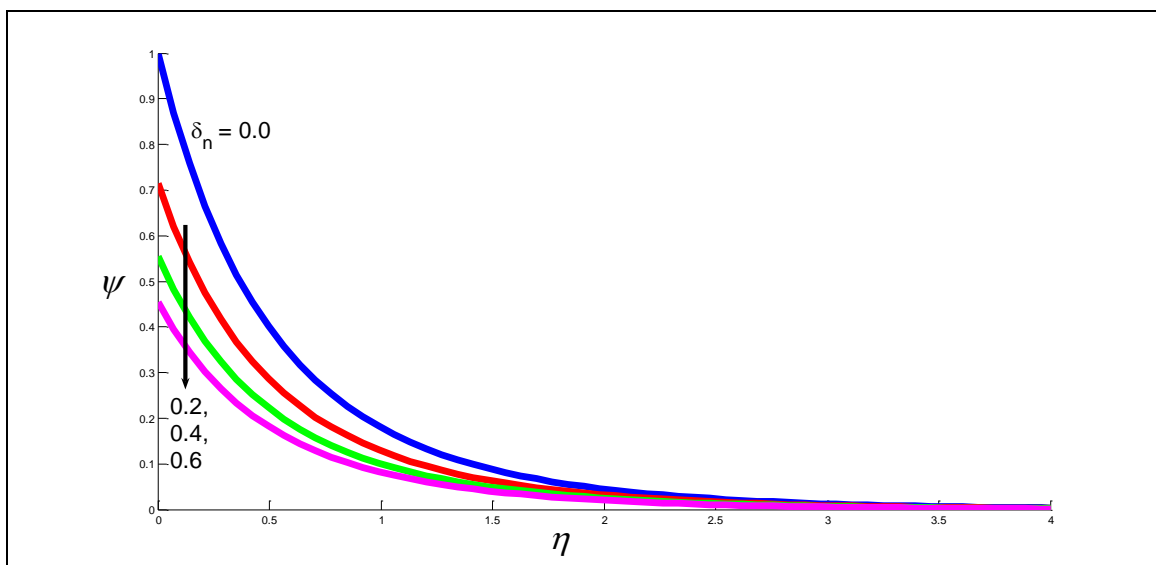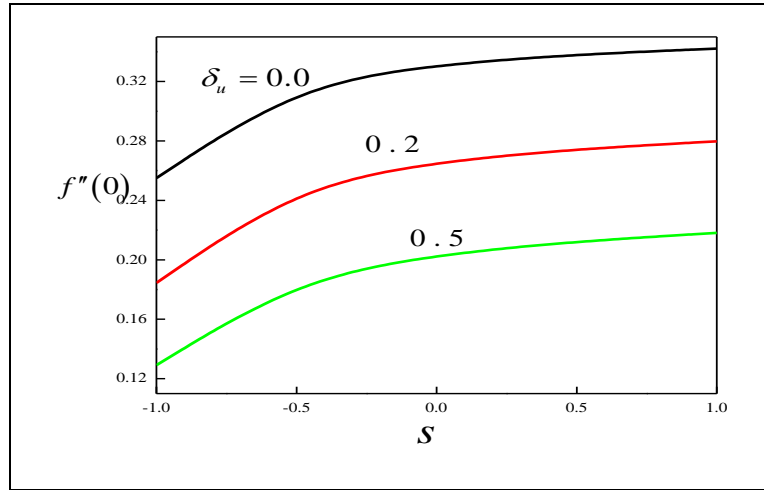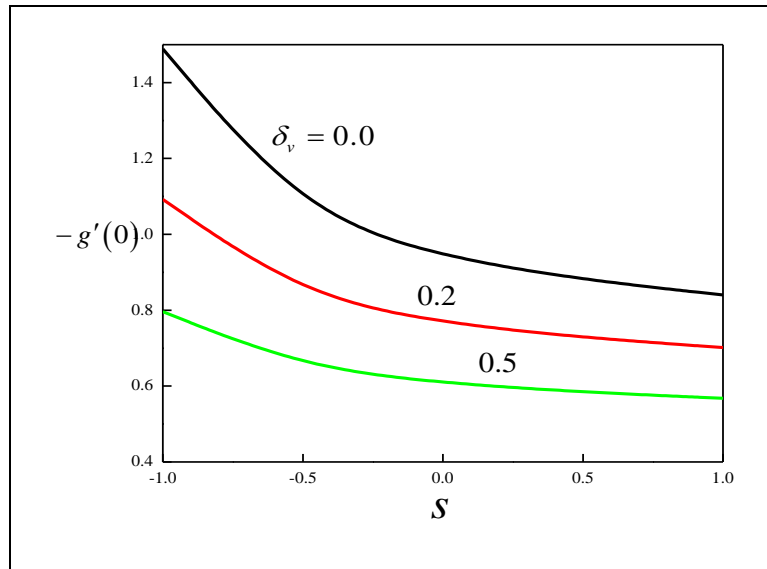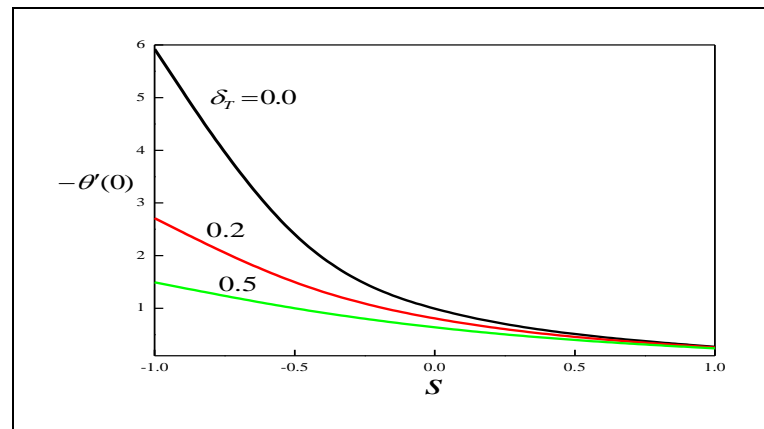
(a)

(b)

(c)

(d)

Figure 10. a) Radial velocity b) temperature c) nanoparticle concentration and d) motile micro-organism density number for different micro-organism slip (δ_n)
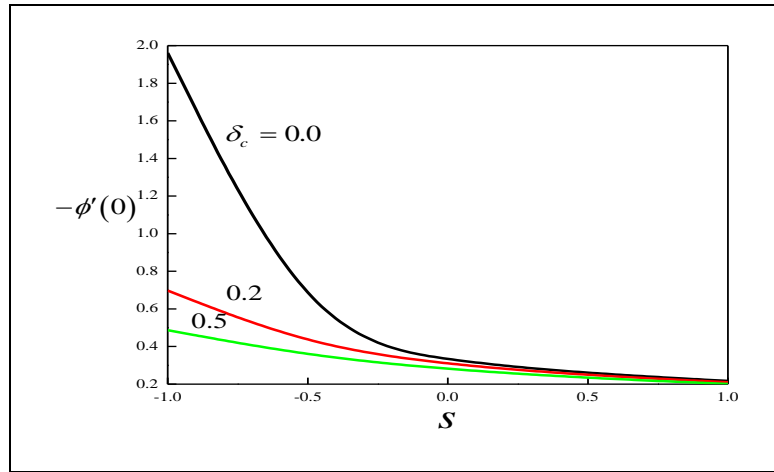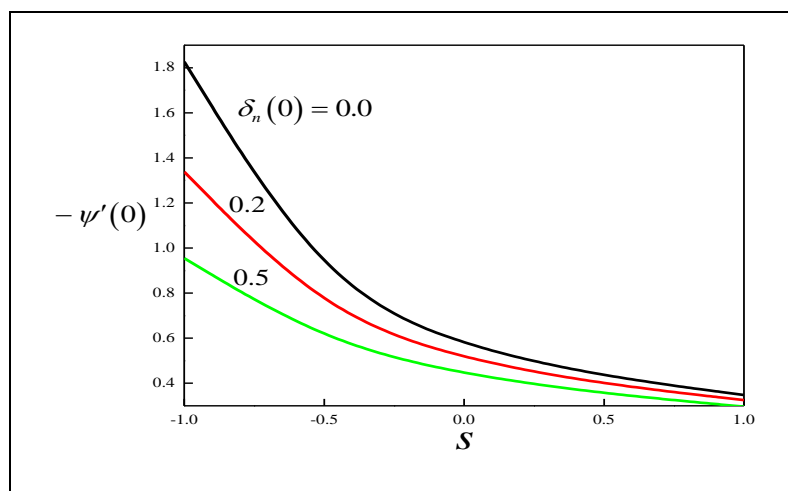
(a)

(b)

(c)

(d)

(e)

Figure 11 a) Radial skin friction b) tangential (circumferential) skin friction c) Nusselt number (wall temperature gradient) d) nanoparticle Sherwood number (wall nanoparticle concentration gradient) e) motile micro-organism density number gradient for different Stefan blowing parameter (s) and slip parameters.

5. CONCLUSIONS

A theoretical study of Von Karman swirling flow of an aqueous nanofluid doped with gyrotactic bioconvecting micro-organisms, from a spinning radially stretching disk to an isotropic permeable medium has been presented as a simulation of bio-inspired nano-coatings for medical devices and implants. Darcy's law is adopted for bulk porous medium drag effects. The Tiwari-Das and Kuznetsov models are adopted for modelling nanofluid and bioconvection phenomena. An additional concentration equation is however included for nanoparticles. Anisotropic hydrodynamic slip (radial and tangential) at the disk surface is included. Stefan blowing is also featured. The transformed dimensionless ordinary differential boundary value problem has been solved numerically with MATLAB bvp4c quadrature. Verification with earlier studies for special cases has been conducted.

Further validation of the general model with the Adomian decomposition method (ADM) is also conducted. Five different nanoparticles have been studied - three metallic and metallic oxides i.e. *silver (Ag), copper (Cu), Titania (TiO₂)* and two carbon-based i.e. *diamond (C) and silicon oxide (SiO₂)*. Graphical plots for the impact of emerging parameters on the transport characteristics i.e. velocity, temperature, nanoparticle concentration, motile micro-organism density number, radial skin friction, tangential skin friction, Nusselt number, nanoparticle Sherwood number and motile micro-organism density gradient have been included. The present simulations have shown that:

(i) Copper-water nanofluid produces the highest nanoparticle concentrations and motile micro-organism density numbers followed by silver, diamond, silicon oxide and finally titanium oxide.

(ii) With increasing volume fraction of copper-water nanofluid and circumferential slip, the radial velocity is strongly depleted, whereas temperature, nanoparticle concentration and motile micro-organism density number are boosted strongly.

(iii) Increasing nanoparticle mass slip strongly elevates radial velocity, temperature, nanoparticle concentration and motile micro-organism density number.

(iv) Increasing radial momentum slip reduces the radial skin friction and increasing tangential slip suppresses the tangential skin friction. Nusselt number, nanoparticle Sherwood number and micro-organism density number gradient are respectively decreased with increment in thermal slip, nanoparticle mass slip and micro-organism slip factors.

(v) Intensification in Stefan blowing accelerates the radial flow and enhances temperature, nanoparticle concentration and micro-organism density number whereas stronger reverse Stefan blowing (suction) induces the opposite effect.

The present investigation has neglected non-Newtonian effects. These may be addressed with a variety of robust rheological models including the Eringen micropolar fluid model [59, 60] and efforts in this regard will be communicated imminently.

References

1. Zhang Z. Biological and Biomedical Coatings Handbook: Processing and Characterization, Advances in Materials Science and Engineering Series. Florida: CRC Press; 2011.

2. Scriven LE. Physics and applications of dip coating and spin coating. MRS Proceedings. 2018; 121:717-729.

3. Kohli R, Mittal KL. Developments in Surface Contamination and Cleaning: Volume 1: Fundamentals and Applied Aspects. 2nd ed. Elsevier; 2016.

4. Später T. Biological coating with platelet-rich plasma and adipose tissue-derived microvascular fragments improves the vascularization, biocompatibility and tissue incorporation of porous polyethylene. Acta Biomaterialia. 2020; 108:194-206.

5. Zandbergen PZ, Dijkstra D. Von Kármán swirling flows. Ann. Rev. Fluid Mech. 1987; 19: 465–491.

6. Ming C, Zheng L, Zhang X. Steady flow and heat transfer of the power-law fluid over a rotating disk. Int. Commun. Heat Mass Transfer. 2011; 38: 280–284.

7. Choi SUS. Enhancing thermal conductivity of fluids with nanoparticles. In: Proceedings of the ASME International Mechanical Engineering Congress and Exposition. San Francisco, USA, 12–17 November, New York; 1995.

8. Lin F. et al. Effective prevention of Escherichia coli biofilm on materials by nano-vibration. Colloids and Surfaces A: Physicochemical and Engineering Aspects. 2021; 608: 125610.

9. Mammeri F. Nanostructured flexible PVDF and fluoropolymer-based hybrid films. Frontiers of Nanoscience. 2019; 14:67-101.

10. Ouyang Y. et al. Nanofluid-infused slippery surface: Bioinspired coating on Zn with high corrosion inhibition performance. Colloids and Surfaces A: Physicochemical and Engineering Aspects. 2021; 608:125492.

11. Çeper T, Arsu N. Photochemically prepared gold/polymer nanocoatings: formation of gold mirror. Macromolecular Chemistry and Physics. 2017; 218: 1700030-1-1700030-8.

12. Yilmaz E, Gulay Ertas, Erman Bengu, Sefik Suzer, Photopatterning of PMMA films with gold nanoparticles: diffusion of $AuCl_4^-$ions. Journal of Physical Chemistry C. 2010; 114: 18401-18406.

13. Hu G. et al. Surface oxidation layer-mediated conformal carbon coating on Si nanoparticles for enhanced lithium storage. ACS Appl. Mater Interfaces. 2021; 13:3991-3998.

14. Montero DA et al. Antimicrobial properties of a novel copper-based composite coating with potential for use in healthcare facilities. Antimicrobial Resistance & Infection Control. 2019; 8: Article number.

15. Buongiorno J. Convective transport in nanofluids. ASME Journal of Heat Transfer. 2006; 128: 240–250.

16. Tiwari RK, Das MK. Heat transfer augmentation in a two-sided lid-driven differentially heated square cavity utilizing nanofluids. International Journal of Heat and Mass Transfer. 2007; 50: 2002-2018.

17. Tassaddiq A. et al. Heat and mass transfer together with hybrid nanofluid flow over a rotating disk. AIP Advances. 2020;10: 055317.

18. Hafeez A. et al. Flow of magnetized Oldroyd-B nanofluid over a rotating disk. Applied Nanoscience. 2020; 10: 5135–5147.

19. Shamshuddin MD, Mishra SR, Bég OA, Bég TA, Kadir A. Computation of radiative Marangoni (thermocapillary) magnetohydrodynamic convection in Cu-water based nanofluid flow from a disk in porous media: smart coating simulation. Heat Transfer. 2021;50:1931-1950.

20. Bhandari DS, Tripathi D. Study of entropy generation and heat flow through a microtube induced by the membrane-based thermoflidics systems. Thermal Science and Engineering Progress. 2022; 34: 101395.

21. Tripathi D, Bhandari DS, Bég OA. Thermal effects on SARS-CoV-2 transmission in peristaltic blood flow: Mathematical modeling. Phys. Fluids. 2022; 34: 061904.

22. Bhandari DS, Tripathi D, Prakash J. Insight into Newtonian fluid flow and heat transfer in vertical microchannel subject to rhythmic membrane contraction due to pressure gradient and buoyancy forces. Int. J. of Heat and Mass Transfer. 2022; 184: 122249.

23. Bees MA. Advances in bioconvection. Ann. Rev. Fluid Mechanics. 2020; 52: 449-476.

24. Bakker DP. et al. Biological micro-organisms feature in numerous technological systems. Colloids Surf. B. 2003;32: 179–190.

25. Ferdows M, Alsenafi A, Bég OA, Bég TA, Kadir A. Numerical study of nano-biofilm stagnation flow from a nonlinear stretching/ shrinking surface with variable nanofluid and bio-convection transport properties. Scientific Reports. 2021;11: 9877-9889.

26. Akram J, SherAkbar N, Alansari M, Tripathi D. Electroosmotically modulated peristaltic propulsion of TiO_2/10W40 nanofluid in curved microchannel. Int. Comm. In Heat and Mass Transfer. 2022; 136: 106208

27. Akram J, Akbar NS, Tripathi D. Analysis of electroosmotic flow of silwer-water nanofluid regulated by peristalsis using two different approaches for nanofluid. J. of Computer Science. 2022; 62: 101696.

28. Sridhar V, Ramesh K, Tripathi D, Vivekanand V. Analysis of thermal radiation, Joule heating, and viscous dissipation effects on blood-gold couple stress nanofluid flow driven by electroosmosis. Heat Transfer. 2022; 51:4080-4101.

29. Akram J, Akbar NS, Tripathi D. Thermal analysis on MHD flow of Ethylene Glycol-based BNNTs nanofluids via peristalticaally induced electroosmotic pumping in a curved microchannel. Arabian J. for Science and Engineering. 2022; 47: 7487-7503.

30. Akram J, Akbar NS, Tripathi D. Entropy generation in electroosmotically aided peristaltic pumping of MoS_2 Robinowitsch nanofluid. Fluid Dynamics Research. 2022; 54: 015507.

31. Akram J, Akbar NS, Tripathi D. Electroosmosis augmented MHD peristaltic transport of SWCNTs suspension in a aqueous media. Journal of Thermal Analysis and Calorimetry. 2022; 147:2509-2526.

32. Tripathi D, Jayavel P, , Bég OA, Srivastava V. EMHD Casson hybrid nanofluid flow over an exponentially accelerated rotating porous surface. J. of Porous Media. doi.org/10.1615/jpormedia.2022041050.

33. Saleem N, Munawar S, Tripathi D. Entropy analysis in ciliary transport of radiated hybrid nanofluid in presence of electromagnetohydrodynamics and activation energy. Case Studies in Thermal Engineering. 2021; 28: 101665.

34. Javid K, Hassan M, Tripathi D, Khan S, Bobescu E, Bhatti MM. Double-diffusion convective biomimetic flow of nanofluid in a complex divergent porous wavy medium under magnetic effects. J. of Biological Physics. 2021; 47:477-498.

35. Tripathi D, Prakash J, Reddy MG, Kumar R. Numerical study of electroosmosis-induced alterations in peristaltic pumping of couple stress hybrid nanofluids through microchannel. Indian J. Physics. 2021; 95:2411-2421.

36. Acharya N. Spectral simulation on the flow patterns and thermal control of radiative nanofluid spraying on an inclined revolving disk considering the effect of nanoparticle diameter and solid-liquid interfacial layer. J. Heat Transfer. 2022; 144:092801.

37. Acharya N, Maity S, Kundu PK. Entropy generation optimization of unsteady radiative hybrid nanofluid flow over a slippery spinning disk. Proceedings of Institute of Mech.Engineers, Part C: J. of Mechanical Engineering. 2022; 236:6007-6024.

38. Acharya N, Bag R, Kundu PK. Unsteady bioconvective squeezing flow with higher-order chemical reaction and second-order slip effects. Heat Transfer. 2021; 1-25. DOI: 10.1002/htj.22137.

39. Acharya N. Spectral quasi linearization simulation on the radiative nanofluid spraying over a permeable inclined spinning disk considering the existence of heat source/sink. Applied Mathematics and Computation. 2021; 411: 126547.

40. Kadir A. et al. Numerical simulation of Von Karman swirling bioconvection nanofluid flow from a deformable rotating disk, ICHTFM. 2018. - 20th International Conference Heat Transfer and Fluid Mechanics, WASET, 16–17 August, Istanbul, Turkey; 2018.

41. Xun S. et al., Bioconvection in rotating system immersed in nanofluid with temperature dependent viscosity and thermal conductivity. Int. J. of Heat and Mass Transfer. 2017; 111: 1001-1006.

42. Waqas H. et al. Bioconvection flow of Casson nanofluid by rotating disk with motile microorganisms. Journal of Materials Research and Technology. 2021; 13: 2392-2407.

43. Khan NS. et al. Entropy generation in bioconvection nanofluid flow between two stretchable rotating disks. Scientific Reports. 2020; 10: Article number 4448.

44. Ngamaramvaranggul V, Webster MF. Simulation of coating flows with slip effects. Int. J. Num. Method Fluids. 2000; 33:961-992.

45. Hayat T, Muhammad T, Shehzad SA, Alsaedi A, On magnetohydrodynamic flow of nanofluid due to a rotating disk with slip effect: a numerical study. Comput. Methods Appl. Mech. Eng. 2017; 315:467-477.

46. Zohra FT, Uddin MJ, Ismail AIM, Beg OA, Kadir A. Anisotropic slip magneto-bioconvection flow from a rotating cone to a nanofluid with Stefan blowing effects. Chinese Journal Physics. 2018; 56: 432-448.

47. Vafai K. Porous Media: Applications in Biological Systems and Biotechnology. Florida: CRC Press, Florida, USA; 2010.

48. Yin C, Zheng L, Zhang C, et al. Flow and heat transfer of nanofluids over a rotating disk with uniform stretching rate in the radial direction. Propulsion Power Res. 2017; 6: 25–30.

49. Bég OA, Uddin MJ, Bég TA, Kadir A, Shamshuddin MD, Babaie M. Numerical study of self-similar natural convection mass transfer from a rotating cone in anisotropic porous media with Stefan blowing and Navier slip. Indian J. Physics. 2020; 94: 863–877.

50. Bég OA, Kabir N, Uddin MJ, Ismail AIM, Alginah Y. Numerical investigation of Von Karman swirling bioconvective nanofluid transport from a rotating disk in a porous medium with Stefan blowing and anisotropic slip effects. Proc. IMechE- Part C- J. Mechanical Engineering Science. 2020; 235:3933-3951.

51. Abu-Nada, E. Application of nanofluids for heat transfer enhancement of separated flows encountered in a backward facing step. Int. J. Heat and Fluid Flow. 2008; 29: 242-249.

52. Chen J, Chen Y, Geng K, Chen, Three-dimensional boundary layer flow over a rotating disk with power-law stretching in a nanofluid containing gyrotactic microorganisms. Heat Transfer – Asian Res. 2018; 47:569-582.

53. Adomian G. Solving Frontier Problems of Physics: The Decomposition Method. Kluwer Academic Publishers. New York;1994.

54. Durual S, Rieder P, Garavaglia G, Filieri ARM, Cattani-Lorente MA, Scherrer SS, Wiskott HA. TiNOx coatings on roughened titanium and CoCr alloy accelerate early osseo integration of dental implants in minipigs. Bone. 2013; 52: 230–237.

55. Bég OA, Tripathi D, Sochi T, Gupta PK. Adomian decomposition method (ADM) simulation of magneto-biotribological squeeze film with magnetic induction effects. J. Mechanics Medicine Biology. 2015; 15:1550072.1-1550072.23.

56. Shamshuddin MD, Mishra SR, Bég OA, Kadir A. Adomian computation of radiative-convective stretching flow of a magnetic non-Newtonian fluid in a porous medium with homogeneous–heterogeneous reactions. Int. J Modern Physics B. 2020; 34: 2050165.

57. Bég OA, Bég TA, Munjam SR, Jangili S. Homotopy and Adomian semi-numerical solutions for oscillatory flow of partially ionized dielectric hydrogen gas in a rotating MHD energy generator duct. Int. J. Hydrogen Energy. 2021;46: 17677-17696.

58. Das SK et al. Nanofluids: Science and Technology. John Wiley, New York, USA: 2007.

59. Ijaz M. et al. Slip flow of micropolar nanofluid over a porous rotating disk with motile microorganisms, nonlinear thermal radiation and activation energy. Int. Comm. in Heat and Mass Transfer. 2021; 122:105161.

60. Bég OA, Vasu B, Ray AK, Bég TA, Kadir A, Leonard HJ, Gorla RSR. Homotopy simulation of dissipative micropolar flow and heat transfer from a two-dimensional body with heat sink effect: applications in polymer coating. Chem. Biochem. Eng. Quart. 2020; 34: 257–275.